A computational aeroelastic framework based on high-order structural models and high-fidelity aerodynamics

Marco Grifò[a], Andrea Da Ronch[b,*], Ivano Benedetti[a,*]

[a] *Department of Engineering, University of Palermo, Viale delle Scienze, Edificio 8, Palermo, 90128, Italy*
[b] *Faculty of Engineering and Physical Sciences, University of Southampton, SO17 1BJ, UK*

Abstract

A computational framework for high-fidelity static aeroelastic analysis is presented. Aeroelastic analysis traditionally employs a beam stick representation for the structure and potential, inviscid and irrotational flow assumptions for the aerodynamics. The unique contribution of this work is the introduction of a high-order structural formulation coupled with a high-fidelity method for the aerodynamics. In more details, the Carrera Unified Formulation coupled with the Finite Element Method is implemented to model geometrically complex composite, laminated structures as equivalent bi-dimensional plates. The open-source software `SU2` is then used for the solution of the aerodynamic fields. The in-house fluid-structure coupling algorithm is based on the Moving Least Square technique. The paper contains a thorough validation of each disciplinary solver of the aeroelastic framework, and provides a few application test cases. For an unswept, untapered and isotropic wing, it was found that the method provides results in agreement with predictions from models based on potential flow theory for moderate freestream velocities. Departures were reported for very low speed and in the high-subsonic regime, alerting the need of adopting high-fidelity flow solutions at these flow conditions. The computational framework was then applied to the static aeroelastic tailoring of a composite wing. The paper concludes providing an overview of future implementation steps towards a tool for the seamless analysis of composite structures subject to different flow conditions, from low to high speed.

Keywords: Composite Structures, Static Aeroelasticity, Fluid-Structure Interaction, Carrera Unified Formulation, Equivalent Plate Modelling, CFD

---

*Corresponding authors
Email addresses: `A.Da-Ronch@soton.ac.uk` (Andrea Da Ronch), `ivano.benedetti@unipa.it` (Ivano Benedetti)

1. Introduction

Fluid-structure interaction is relevant to any engineering system exposed to a flow, from industrial high risers, bridges and wind turbines to aircraft, propeller and wind turbine blades [1, 2, 3, 4]. In the context of aeronautics, the study of fluid-structure interaction is commonly referred to as aeroelasticity. The objectives of aeroelastic analysis and design are the assessment of the load redistribution due to the coupling between structural deformation and aerodynamic loads and the prevention of static and dynamic aeroelastic phenomena, such as divergence and flutter, respectively [5, 6, 7]. These activities are critical from the very early stages of the design process until the detailed design. The present work is devoted to the development of a high-order/high-fidelity computational tool for static aeroelastic analysis of composite structures.

The use of composite materials and structures has become increasingly attractive, especially in the aerospace sector, because of their remarkable stiffness/strength-to-weight ratios, fatigue resistance, environmental and chemical stability, and the wide design space they offer, which is reflected in a remarkable flexibility of structural applications [8, 9]; in the aircraft and aerospace sectors, *Aeroelastic Tailoring* [10] is one of the most attractive possibilities offered by composite materials, from the traditional Constant Stiffness Composite Laminates (CSCLs) to the more recent Variable Angle Tow (VAT) composites, which allow concentrating strength and specific properties in predetermined directions where these are required (such as bending strength in bending dominated regions or traction strength in traction dominated ones). The state-of-the-art in aeroelastic tailoring is discussed in [11] and some examples about aeroelastic tailoring of composite wings can be found in [12, 13].

To fully exploit the potential advantage of a wide design space, the use of suitable, reliable and robust analytical, numerical and computational tools for structural analysis [14] is highly desirable. This would also limit the need, and particularly the cost, of contingent experimental campaigns. In general, composites are modelled employing Equivalent Single Layer (ESL) or Layer-Wise (LW) models, according to the need to recover less or more accurately the transverse mechanical fields. To perform the aeroelastic analysis of a structural component, a suitable aerodynamic model and an algorithm to couple the two fields – the structural and the aerodynamic field – are needed.

For aeroelastic analysis and design performed at the conceptual/preliminary phase, composite wings are investigated employing either beam [15] or plate [16] structural models. The Finite Element Method (FEM) [17] is often adopted for the discretization of the structural equations and typically provides a set of structural matrices modelling the elastic, damping and inertial features of the considered components, with a number of degrees of freedom (DOFs) depending on the kinematic assumptions and thus on the required level of prediction accuracy. Recently, the *Carrera Unified Formulation* (CUF) [18] has emerged as a powerful general framework for the automatic generation of structural theories of variable order for the analysis of either homogeneous or laminated structures. In CUFs, the order of expansion of the kinematic model appears as an input parameter, so that the adequacy and accuracy of structural theories of different orders can be cross-assessed with respect to specific applications.

Both one-dimensional (1D) and two-dimensional (2D) CUFs have been developed for aeroelastic analysis, with 1D (beam) models based on the use of 2D cross-section functions $F_k\left(\xi,\eta\right)$, expressing the assumed behaviour of the unknown fields over the transverse section [19], as opposed to through-the-thickness 1D functions $F_k\left(\xi\right)$ adopted for analogous purposes in 2D models. In such formulations, the integration over variable thickness structures is reminiscent of the techniques employed in Equivalent Plate Modelling, obtained for example by the application of the Ritz method as in Ref.[20]. In this work, a 2D CUF is developed for the analysis of wings exhibiting airfoil sections and complex structural layout.

From the aerodynamic point of view, beam and plate models are often coupled with low fidelity aerodynamic theories, which favour simplicity and low computational costs over accuracy and result adequate for conceptual design purposes. The Vortex Lattice Method (VLM) and the Doublet Lattice Method (DLM) employed, respectively, for steady and unsteady problems, see e.g. Ref.[21], provide remarkable examples in this sense: they yield an approximate distribution of fluid velocity and pressure over the analysed structure, that is then transferred to the structural model through Spline Methods [22] or other Fluid-Structure Interaction (FSI) strategies [23], providing results at low computational cost with engineering accuracy.

A large body of work has been devoted to the analysis of beams and plates under aerodynamic loads calculated using low-fidelity models for static and dynamic problems. Beam models of different orders for high-aspect ratio wings in both static and dynamic regimes have been developed employing either VLM or DLM [24, 25, 26, 27]. In beam models, complex and possibly three-dimensional structural effects, encountered for example in *low* aspect-ratio wings with complex cross sections, may be investigated employing a subdivision of the cross sections in subdomains and enriching the discretization through additional cross-section functions $F_k(\xi,\eta)$, often provided by Lagrange polynomials or hierarchical Legendre functions, see e.g. Ref.[28]. In such cases, plate models [29, 30] offer a valid structural alternative and may become competitive, in terms of number of structural degrees of freedom, with respect to beam models with highly refined kinematic assumptions. A further advantage of plate models is provided by simpler through-the-thickness integration procedures for the computation of the stiffness terms. Equivalent Plate Models have been employed to analyze multi-plate models with the Ritz method and penalty function techniques [31] or with the finite elements method (FEM) [32]. A recent plate wing application can be found in Ref.[33] for aeroelastic design, and in Ref.[34], where FEM with Reduced Order Models (ROMs) are employed for a staggered static aeroelastic analysis.

An example of advanced aeroelastic analysis based on Computational Fluids Dynamics (CFD) is provided in Ref.[35], where aerodynamic uncertainties of RANS equations are reflected in possible aeroelastic deficiencies in the design process of an Unmanned Combat Air Vehicle (UCAV). The coupling between the aerodynamic and structural models is ensured by a scheme based on a Moving-Least Square (MLS) patches technique, as presented in Ref.[23]: the mesh-free approach allows managing easily the coupling issue, guaranteeing the conservation of momentum and energy transfer between the two domains, according to the Principle of Virtual Displacements (PVD).

In general, low-fidelity aerodynamic models, such as VLM and DLM, are unable to capture viscous effects that are present at both low-velocity and high-velocity flight, as well as high angles of attack. They also show limitations in very low-velocity aerodynamic ranges, where the Reynolds number becomes too low and viscosity effects cease to be negligible, as well as in the analysis of blunt geometries [21]. From the literature survey, it emerges that CUF beam or plate formulations, which represent a class of *higher-order* structural models, have generally been used in conjunction with simplified aerodynamic models, but there are no examples of coupling with *high-fidelity* CFD, that could be useful to investigate either high or very low-velocity aerodynamic regimes.

The use of high-fidelity CFD in aeroelastic modelling generally requires the adoption of staggered approaches, in which the aerodynamic problem and the structural problem are sequentially solved and information is passed from the aerodynamics to the structure, in terms of loading, and from the structure to the aerodynamics, in terms of updated boundary geometry, through deformation and updated displacements, for the updating of the sequential solution steps, until aerodynamics/structural convergence is reached. In general, since the aerodynamic influence coefficient (AIC) matrices are not readily available, the eigenvalue solution to the divergence or flutter problems are not possible, and the instability conditions must be explicitly searched. Although such staggered approaches are generally more costly in terms of computational resources, they have been recently successfully adopted [36, 37]. On the other hand, if flexible CFD and fluid-structure coupling routines are adopted, staggered approaches can be straightforwardly extended to the study of general aerodynamic regimes, either in the very low-velocity or transonic/supersonic regime, or cases involving flow separations, e.g. at high angles of attack.

The present work focuses on the development of an aeroelastic framework that employs a high-order structural model and a high-fidelity aerodynamic model. In particular, a higher-order Equivalent Plate Model (EPM) is built employing generalized CUF kinematic assumptions, whose order may be enriched exploiting the generality of the CUF, and solved through FEM; the aerodynamics is modelled employing the open-source suite `SU2` [38], a collection of `C++` based software tools for Partial Differential Equation (PDE) analysis and PDE-constrained optimization problems, mainly designed for CFD and aerodynamic shape optimization. The interface between the structural and aerodynamic models is built using a Moving-Least Square (MLS) patches technique, as presented in Ref.[23]. The proposed CUF/FEM/EPM/CFD aeroelastic tool aims, in the long term, at achieving a high level of generality in terms of structural configurations that are modelled (low to high aspect ratio wings, homogeneous and composite, with and without internal stiffening elements) and of the aerodynamic regime that is analysed.

The work is organised as follows. Section 2 describes in detail the development of the structural model, introduces the `SU2` suite, reviews the main CFD assumptions and discusses the adopted fluid-structure coupling routines. Section 3 validates the developed model against available reference data and presents the results of an aeroelastic tailoring analysis. Section 4 critically discusses some aspect of the developed tool and highlight future steps of investigation, before *Conclusions* are drawn.

2. Aeroelastic formulation

In the literature, the aeroelastic response of composite structures is often studied employing fast but simplified aerodynamic models, e.g. VLM or DLM, coupled with more or less sophisticated structural models [39, 36, 6]. In this work, a high-order structural model [40] is coupled with a high-fidelity aerodynamic description for the static aeroelastic analysis of homogeneous and composite structures. This section provides a description of the disciplinary software tools employed in this work. First, the structural model, formed using a CUF-FEM based variable-order equivalent plate formulation, is described in detail. Then, the open-source aerodynamic solver, `SU2`, is briefly overviewed. The structural and aerodynamic solvers are coupled by a dedicated interface, whose description concludes the section. The eager reader is referred to references contained herein for in-depth details.

2.1. Structural model

The structural model is based on generalized kinematic assumptions and on the finite element discretization of the resulting equations, built starting from the weak formulation of the structural problem obtained from the principle of virtual displacements. The generalized stiffness contributions are computed by suitable integration over regions with variable material/geometry distribution, which eventually generate the equivalent plate model.

2.1.1. Kinematics assumptions

A generic three-dimensional (3D) structure, for example a wing, occupying the volume $\hat{\mathbb{V}} \in \mathbb{R}^3$ is considered: such a structure is enclosed by a well defined external surface S and may contain internal stiffening elements such as stringers or ribs.

The first essential item of the formulation is the adoption of a general variable-order kinematic assumption written with reference to a flat *modelling domain* $\hat{\Omega} \in \mathbb{R}^2$, identified as a reference domain for the whole structure; in the case of a wing, $\hat{\Omega}$ could lay, for example, within the plane perpendicular to the aircraft symmetry plane containing the wing root section chord and its boundary $\hat{\Gamma} \equiv \partial\hat{\Omega}$ could be identified by the projection of the structure along the direction normal to such plane itself. In this scenario, the *i-th* component of displacement for the generic point $\hat{\mathbf{x}} \equiv (\hat{x}_1, \hat{x}_2, \hat{x}_3) \in V$ is expressed as

$$u_i\left(\hat{x}_1, \hat{x}_2, \hat{x}_3\right) = \sum_{\alpha=0}^{N_{u_i}} u_{i\alpha}\left(\hat{x}_1, \hat{x}_2\right) f_\alpha\left(\hat{x}_3\right) \qquad i = 1, 2, 3 \tag{1}$$

where $(\hat{x}_1, \hat{x}_2) \in \hat{\Omega}$, x_3 identifies the direction normal to the flat modelling domain $\hat{\Omega}$, $f_\alpha\left(\hat{x}_3\right)$ represents *known* through-the-thickness functions, $u_{i\alpha}\left(\hat{x}_1, \hat{x}_2\right)$ are *unknown* generalized displacement functions and $N_{u_i} + 1$ is the order of expansion associated with the displacement component u_i. Eq.(1) can also be recast in a more compact matrix form, suitable for computer implementation, as

$$\boldsymbol{u}\left(\hat{\mathbf{x}}\right) = \mathbf{F}\left(\hat{x}_3\right) \boldsymbol{U}\left(\hat{x}_1, \hat{x}_2\right) \tag{2}$$

where $\mathbf{F}(\hat{x}_3)$ is a $3\times(3+N_{u_1}+N_{u_2}+N_{u_3})$ matrix depending only on $\hat{x}_3$, while $\boldsymbol{U}(\hat{x}_1,\hat{x}_2)$ contains all the unknown generalized functions.

Various structural theories may be obtained selecting the appropriate functions $f_\alpha(\hat{x}_3)$ and orders of expansion for different displacement components. The First order Shear Deformation Theory (FSDT) [41, 42] is retrieved, for example, by setting $f_\alpha(\hat{x}_3)=\hat{x}_3^\alpha$, $N_{u_1}=N_{u_2}=1$ and $N_{u_3}=0$. Higher-Order Shear Deformation Theories are obtained increasing N_{u_1}, N_{u_2} and penalizing N_{u_3}, as shown for example in [43], where the in-plane warping of fibers in composite laminates is investigated. Higher-order theories (HOT) can be obtained increasing the order of expansion for all the displacement components.

Strains ε_{ij} and stresses σ_{ij} are associated with the displacements given by Eq.(1) by the standard strain-displacements relationship and constitutive equations

$$\varepsilon_{ij}=\frac{1}{2}\left(u_{i,j}+u_{j,i}\right),\qquad \sigma_{ij}=C_{ijkl}\varepsilon_{kl}, \tag{3}$$

which may also be expressed in matrix format as

$$\boldsymbol{\varepsilon}=\mathscr{D}\boldsymbol{u}=\mathbf{I}_k\mathbf{F}\frac{\partial\boldsymbol{U}}{\partial\hat{x}_k}+\mathbf{I}_3\frac{d\,\mathbf{F}}{d\hat{x}_3}\boldsymbol{U},\qquad \boldsymbol{\sigma}=\mathbf{C}\boldsymbol{\varepsilon}, \tag{4}$$

where $\boldsymbol{\varepsilon}$ and $\boldsymbol{\sigma}$ are 6×1 vectors containing the components of the strain and stress tensors in Voigt notation and the strain-displacement linear differential operator $\mathscr{D}$ has been written as

$$\mathscr{D}=\mathbf{I}_1\frac{\partial(\cdot)}{\partial\hat{x}_1}+\mathbf{I}_2\frac{\partial(\cdot)}{\partial\hat{x}_2}+\mathbf{I}_3\frac{\partial(\cdot)}{\partial\hat{x}_3}=\mathbf{I}_k\frac{\partial(\cdot)}{\partial\hat{x}_k}+\mathbf{I}_3\frac{\partial(\cdot)}{\partial\hat{x}_3}, \tag{5}$$

where the Einstein implicit summation convention over $k=1,2$ is adopted at the right hand side and the matrices $\mathbf{I}_1$, $\mathbf{I}_2$ and $\mathbf{I}_3$ are 6×3 matrices containing zeros and ones, so to fulfill the identity in Eq.(5).

2.2. Discrete structural equations

Once the kinematic model in Eq.(1) or Eq.(2) is adopted, the discrete solving equations are written by invoking a suitable variational statement, e.g. the Principle of Virtual Displacements (PVD) for static problems, and introducing a suitable finite elements discretization of the analysis domain. In matrix format, the PVD reads

$$\delta\mathscr{L}_{int}=\int_{\hat{V}}\delta\boldsymbol{\varepsilon}^\mathsf{T}\boldsymbol{\sigma}\,dV=\int_{\hat{S}}\delta\boldsymbol{u}^\mathsf{T}\boldsymbol{t}\,dS=\delta\mathscr{L}_{ext} \tag{6}$$

where the volume forces have been neglected and $\boldsymbol{t} = \mathscr{D}_n^{\intercal}\boldsymbol{\sigma}\ \forall \mathbf{x} \in S$, with the discrete operator obtained from the differential strain-displacement operator $\mathscr{D}$ by replacing $\partial(\cdot)/\partial x_i$ with n_i, i.e. the *i-th* component of the unit outward normal vector in $\mathbf{x}$.

Introducing Eq.(2) into the expression of the virtual internal work, yields

$$\delta\mathscr{L}_{int} = \int_V \left(\frac{\partial \delta \boldsymbol{U}^{\intercal}}{\partial \hat{x}_i} \mathbf{F}^{\intercal} \mathbf{C}_{ij} \mathbf{F} \frac{\partial \boldsymbol{U}}{\partial \hat{x}_j} + 2\delta \boldsymbol{U}^{\intercal} \frac{d\,\mathbf{F}^{\intercal}}{d\hat{x}_3} \mathbf{C}_{3i} \mathbf{F} \frac{\partial \boldsymbol{U}}{\partial \hat{x}_i} + \delta \boldsymbol{U}^{\intercal} \frac{d\,\mathbf{F}^{\intercal}}{d\hat{x}_3} \mathbf{C}_{33} \frac{d\,\mathbf{F}}{d\hat{x}_3} \boldsymbol{U} \right) dV \tag{7}$$

where $\mathbf{C}_{ij} = \mathbf{I}_i^{\intercal}\mathbf{C}\mathbf{I}_j$ and the implicit summation is assumed over the subscripts $i, j = 1, 2$. After discretizing the domain $\hat{\Omega}$ into a collection of non-overlapping elements $\hat{\Omega}_e \in \omega \in \mathbb{R}^2$, according to classical FE procedures, introducing over each element the coordinate transformation $\hat{x}_i = \hat{x}_i(\xi, \eta)$, $i = 1, 2$, and the expression of the generalized variables $\boldsymbol{U}$ in terms of shape functions $\mathbf{N}(\xi, \eta)$ and nodal values $\hat{\mathbf{U}}_e$, the integral in Eq.(7) can be written as

$$\delta\mathscr{L}_{int} = \sum_{e=1}^{N_e} \delta\hat{\mathbf{U}}_e^{\intercal}\, \mathbf{K}_e\, \hat{\mathbf{U}}_e \tag{8}$$

where

$$\mathbf{K}_e = \int_{\Omega_e} \int_t \left(\frac{\partial \mathbf{N}^{\intercal}}{\partial \hat{x}_i} \mathbf{F}^{\intercal} \mathbf{C}_{ij} \mathbf{F} \frac{\partial \mathbf{N}}{\partial \hat{x}_j} + 2\mathbf{N}^{\intercal} \frac{d\,\mathbf{F}^{\intercal}}{d\hat{x}_3} \mathbf{C}_{3i} \mathbf{F} \frac{\partial \mathbf{N}}{\partial \hat{x}_i} + \mathbf{N}^{\intercal} \frac{d\,\mathbf{F}^{\intercal}}{d\hat{x}_3} \mathbf{C}_{33} \frac{d\,\mathbf{F}}{d\hat{x}_3} \mathbf{N} \right) d\hat{x}_3\, d\hat{\Omega}, \tag{9}$$

is a $3 \times N_n^e \times (1 + N_u)$ matrix, assuming that N_n^e is the number of nodes associated with the element e and that the same expansion order N_u has been assumed for the three components of displacements in Eq.(1), and $t = t(\hat{x}_1, \hat{x}_2)$ indicates the integration interval in the thickness direction, which in general depends on the specific location over the domain $\hat{\Omega}$. The above expression can be further simplified observing that only $\mathbf{F}$ and, potentially, $\mathbf{C}$ depend on $\hat{x}_3$, thus yielding

$$\mathbf{K}_e = \int_{\Omega_e} \left(\frac{\partial \mathbf{N}^{\intercal}}{\partial \hat{x}_i} \tilde{\mathbf{F}}_{ij} \frac{\partial \mathbf{N}}{\partial \hat{x}_j} + 2\mathbf{N}^{\intercal} \tilde{\mathbf{F}}'_{3i} \frac{\partial \mathbf{N}}{\partial \hat{x}_i} + \mathbf{N}^{\intercal} \tilde{\mathbf{F}}''_{33} \mathbf{N} \right) d\Omega, \tag{10}$$

where $\tilde{\mathbf{F}}_{ij}(\hat{x}_1, \hat{x}_2)$, $\tilde{\mathbf{F}}'_{3i}(\hat{x}_1, \hat{x}_2)$ $\tilde{\mathbf{F}}''_{33}(\hat{x}_1, \hat{x}_2)$ are defined by

$$\tilde{\mathbf{F}}_{ij} = \int_t \mathbf{F}^{\intercal} \mathbf{C}_{ij} \mathbf{F}\, d\hat{x}_3 \qquad \tilde{\mathbf{F}}'_{3i} = \int_t \frac{d\,\mathbf{F}^{\intercal}}{d\hat{x}_3} \mathbf{C}_{3i} \mathbf{F}\, d\hat{x}_3 \qquad \tilde{\mathbf{F}}''_{33} = \int_t \frac{d\,\mathbf{F}^{\intercal}}{d\hat{x}_3} \mathbf{C}_{33} \frac{d\,\mathbf{F}}{d\hat{x}_3}\, d\hat{x}_3. \tag{11}$$

The structure of the through-the-thickness expansion matrix $\mathbf{F}(x_3)$ and of the shape functions matrix $\mathbf{N}(\xi, \eta)$ allow expressing Eqs.(10)-(11) in a form particularly suitable for matrix implementation. It may be shown for example that

$$\tilde{\mathbf{F}}_{ij} = \int_t \left(\boldsymbol{\phi}^{\intercal} \otimes \mathbf{C}_{ij} \otimes \boldsymbol{\phi} \right) d\hat{x}_3 \tag{12}$$

and that

$$\int_{\Omega_e} \left(\frac{\partial \mathbf{N}^\intercal}{\partial \hat{x}_i} \tilde{\mathbf{F}}_{ij} \frac{\partial \mathbf{N}}{\partial \hat{x}_j} \right) d\Omega = \int_{\hat{\Omega}_e} \left(\frac{\partial \boldsymbol{\psi}^\intercal}{\partial \hat{x}_i} \otimes \tilde{\mathbf{F}}_{ij} \otimes \frac{\partial \boldsymbol{\psi}}{\partial \hat{x}_j} \right) d\hat{\Omega} \tag{13}$$

where the symbol $\otimes$ indicates the Kronecker product, $\boldsymbol{\phi}(\hat{x}_3) = (f_0, f_1, \dots, f_N)$ is a $1 \times (1+N)$ vector collecting the through-the-thickness expansion functions appearing in Eq.(1), $\boldsymbol{\psi}(\xi, \eta) = \left(N_1, N_2, \dots, N_{N_n^e}\right)$ is a $1 \times N_n^e$ vector collecting the shape functions $N_k(\xi, \eta)$ employed to describe the fields over the considered element. As a consequence, it may be observed that the matrix in Eq.(13) is assembled by 3×3 matrix blocks of the generic form

$$\mathbf{B}_{\alpha\beta}^{kl} = \int_{-1}^{+1} \int_{-1}^{+1} \frac{\partial N_k}{\partial \hat{x}_i} \left[\int_t (f_\alpha \mathbf{C}_{ij} f_\beta)\, d\hat{x}_3 \right] \frac{\partial N_l}{\partial \hat{x}_j} J(\xi, \eta)\, d\xi d\eta, \tag{14}$$

where $J(\xi, \eta)$ is the Jacobian of the trasnformation $\hat{x}_i = \hat{x}_i(\xi, \eta)$, $i = 1, 2$, suitably collocated within $\mathbf{K}_e$, according with the subscripts (α, β), related with the through-the-thickness expansion order, and (k, l), related with the shape functions.

Analogous generic relationships may be built also for the other terms appearing in Eq.(10); due to the explicit dependence on the order of the expansion of the kinematic model, such *fundamental blocks* allow generalizing the formulation to variable-order kinematics. It is worth observing that further simplifications are possible if the analyzed structure is made of a single homogeneous material and in regions where the through-the-thickness integration interval t is constant, i.e. does not depend on $(\hat{x}_1, \hat{x}_2)$, see e.g. Ref.[44].

Similarly, employing Eq.(1), the virtual external work can be written

$$\delta \mathscr{L}_{ext} = \sum_{e=1}^{N_e} \delta \hat{\mathbf{U}}_e^\intercal \boldsymbol{f}_e \tag{15}$$

with

$$\boldsymbol{f}_e = \int_{S_e} \mathbf{N}^\intercal \mathbf{F}^\intercal \boldsymbol{t}(\hat{\mathbf{x}})\, dS = \int_{S_e} \left(\boldsymbol{\psi}^\intercal \otimes \boldsymbol{\phi}^\intercal \otimes \boldsymbol{t} \right) dS \tag{16}$$

where $\boldsymbol{t}(\hat{\mathbf{x}})$ is the surface load, in general due to both pressure and frictional contributions, provided by the computational aerodynamic tool, see Section 2.3. The above expression can be explicitly computed, for upper and lower structural surfaces admitting a regular parametric representation with respect to $\hat{\Omega}_e$, assembling elementary 3×1 blocks of the form

$$\boldsymbol{f}_e = \int_{-1}^{+1} \int_{-1}^{+1} N_k(\xi, \eta)\, f_\alpha [\hat{x}_3(\xi, \eta)]\, \boldsymbol{t}[\hat{\mathbf{x}}(\xi, \eta)] J_S(\xi, \eta)\, d\xi d\eta \tag{17}$$

where the Jacobian $J_S(\xi, \eta)$, different from $J(\xi, \eta)$ appearing in Eq.(14), is defined by $dS = J_S(\xi, \eta)\, d\xi d\eta$. Other specialized expressions should be used for walls vertical with respect to Ω_e.

Considering Eq.(10) and Eq.(15), the method leads, for static problems, to a system of the classical form

$$\mathbf{K}\hat{\mathbf{U}} = \mathbf{F}. \tag{18}$$

The assembly procedure for the matrix $\mathbf{K}$ and vector $\mathbf{F}$ consists of a hierarchical distribution/ superposition of fundamental blocks of the form given in Eq.(14) or Eq.(17), first in *nodal*, then in *elemental* and thus in *global* stiffness matrices and nodal force vectors.

For laminated composite plates, treated within the ESL framework, each lamina is computed and then node-wisely superimposed to the others. In thin plates the *Poisson locking* [17] could introduce a non-negligible solution error, because of an overestimation of the shear stiffness terms. To solve this issue, *selective reduced integration* is often employed [45]: the terms of the element stiffness matrix are obtained summing up in-plane and out-of-plane components, separately integrated considering just one quadrature point for out-of-plane components and four quadrature points for the in-plane components.

For more complex structures, see e.g. Fig.(1), the stiffness matrix is computed considering the material distribution along x_3, so that the contribution of spars, ribs, skin or other generic components can be included in the model integrating the through-the-thickness terms of the integrand functions in Eq.(14) or Eq.(17) over the real physical configuration of the solid, and then adding such contributions as discussed e.g. in Ref.[46]. Of course, when the integration of wing configurations with aerodynamically shaped transverse sections is addressed, care must be devoted to the implementation of robust integration routines, to avoid inaccuracies at the leading or trailing edges, which generally exhibit high curvature or other specific morphological features.

2.3. Aerodynamic Model

Herein, CFD is used as source of the aerodynamic loads that are applied to the flexible structure. The flow is analysed within a discretised 3D control volume. The growth of the surface mesh on the control volume depends on the value of y^+ [47], a non-dimensional measure of the viscous sublayer which is directly proportional to the friction velocity u_τ and the dimensional distance from the wall y, and inversely proportional to kinematic viscosity ν:

$$y^+ = \frac{y u_\tau}{\nu} \tag{19}$$

Convergence tests need to be carried out to ensure independence of the results on the value of y^+, the extension of the farfield from the model geometry and the growth rate of the volume mesh

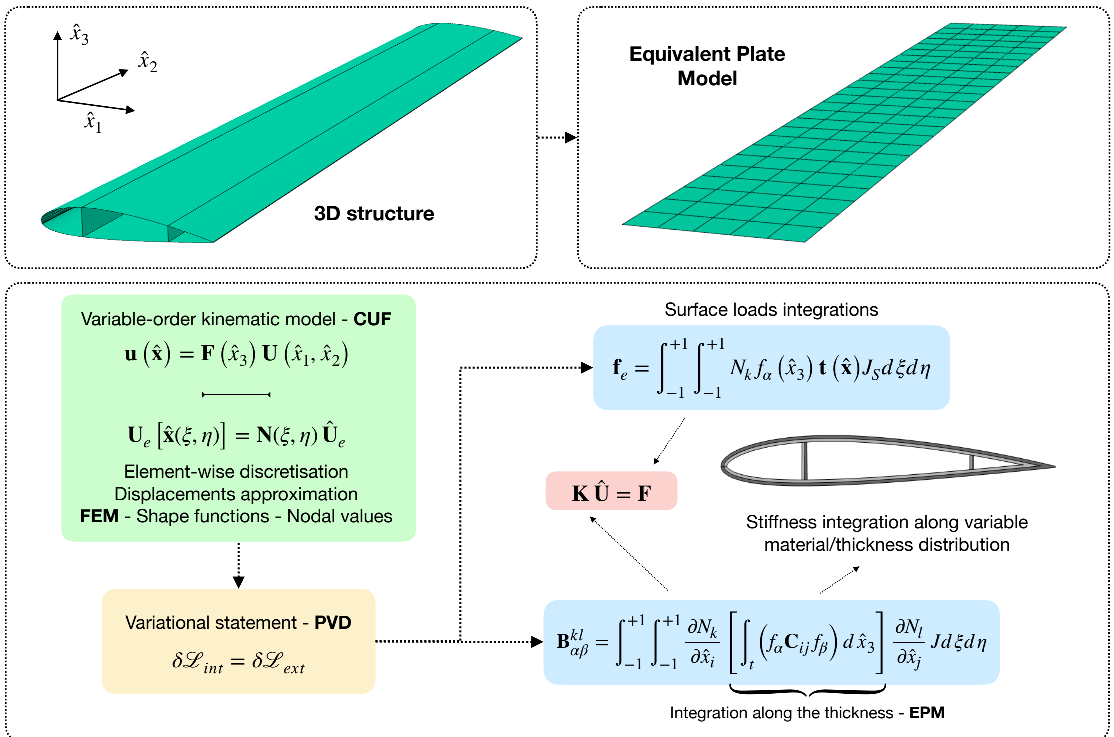

Figure 1: Schematic representation of the structural model: the generalized kinematic model, compounded with standard FE approximations, leads to the Equivalent Plate Model through integration of the stiffness matrix contributions over regions with variable material/geometry distribution.

within the viscous sublayer. General guidelines can be found, for example, in Ref.[48]. Herein, convergence tests were run on three grids of different spatial discretisation (see Section 3.2).

Aerodynamic predictions are obtained using `SU2` [49]. In this work, the laminar model and the Spalart-Allmaras (SA) turbulence model [50] were used. The SA model provides an additional equation for the transport of turbulent viscosity. Other models, such as $k-\omega$ [51], were used initially for the validation study presented in Section 3.2.

In the CFD framework, a surface $\check{\Omega} \in \mathbb{R}^2$ is defined as the boundary wall of the model geometry, placed inside the volume domain $\check{\mathbb{V}} \in \mathbb{R}^3$. The reference system $\check{\mathbf{x}} = (\check{x}_1, \check{x}_2, \check{x}_3)$ represents the local orientation for the volume $\check{\mathbb{V}}$. The Finite Volume Method is employed to solve the governing equations in $\check{\mathbb{V}}$ through Jameson–Schmidt–Turkel (JST) convective scheme [52] for the convective fluxes through the element edges, with the second and fourth order dissipation coefficients of 0.2 and 0.05, respectively. A residual convergence criteria is adopted, with a Flexible Generalized Minimum Residual (FGMRES) method as linear solver [53]. When turbulence models are introduced, a general scalar upwind method is chosen as convective scheme.

The term $\boldsymbol{t}(\hat{\mathbf{x}})$, mentioned in Section 2.1, represents the surface loads applied onto the structural mesh points. It comes from `SU2` output as c_p, $c_{f\check{x}_1}$ and $c_{f\check{x}_2}$ values which are, respectively, the pressure coefficient and the skin friction coefficients. These coefficients are associated to the reference system $\check{\mathbf{x}}$, and are given node-wisely on the CFD geometrical mesh that discretizes the $\check{\Omega}$ surface. The skin friction is calculated after having established precise assumptions for the viscosity model. In this work, Sutherland law [54] is adopted to define the dependency of the viscosity from the temperature. Once defined the main thermodynamic properties of the fluid, such as ρ_∞ and V_∞, respectively, freestream density and freestream velocity of the flow, the CFD simulation is launched. In the output produced by `SU2` the coefficients are node-wisely listed, and are thus employed as in Eq. (20) to reconstruct the loading traction components in the CFD reference system $\check{\mathbf{x}}$:

$$\mathbf{t}(\check{\mathbf{x}}) = \frac{1}{2}\rho_\infty V_\infty \mathbf{c}(\check{\mathbf{x}})\,\mathbf{n}(\check{\mathbf{x}}) \tag{20}$$

where $\mathbf{c}(\check{\mathbf{x}})$ contains the vectors c_p, $c_{f,\check{x}_1}$ and $c_{f,\check{x}_2}$ ordered according to the numeration of the aerodynamic mesh, and $\mathbf{n}(\check{\mathbf{x}})$ is the vector containing the components of every normal vector ordered consistently with the numeration of the aerodynamic mesh.

The subsequent step involves the transfer of $\mathbf{t}(\check{\mathbf{x}})$ in the structural mesh defined in the $\hat{\mathbf{x}}$ reference system. This process follows the sequence of steps outlined in Section 2.4.

2.4. Fluid-structure Interaction

The coupling between two general-purpose solvers for the structural and aerodynamics fields require a dedicated fluid-structure interaction (FSI) algorithm to facilitate the exchange of information between the two fields. The FSI algorithm ensures that the transfer of load and displacement fields from one domain to the other is conservative in terms of momentum and energy, without introducing spurious energy or any dissipation. Herein, the Moving-Least Square (MLS) patches technique [23] is used. It is a suitable approach for heterogeneous fluid-structure strategies. The quality of the MLS approximation is determined by the definition of radial basis functions (RBF) that establish the kind of interpolation made among points of different discretised domains [35].

The FSI matrix, often denoted $\mathbf{H}$ in the literature, allows calculating the equivalent variable field of a domain in another domain. This equivalence is made possible by defining an equivalence of the Virtual Works from the two domains, Eq.(21a), and the minimisation of a mean least square error calculated on two displacement fields of the two distinct domains weighted on the RBFs, Eq.(21b).

$$\begin{gathered}\sum_{k=1}^{\hat{N}} \mathbf{F}_k \cdot \left(\delta \hat{\mathbf{U}}\right)_k = - \int_{\check{\Omega}} \mathbf{t}\left(\check{\mathbf{x}}\right) \cdot \sum_{m=1}^{\check{N}} S_i \sum_{k=1}^{\hat{N}} h_{ij} \left(\delta \hat{\mathbf{U}}\right)_m \, d\mathbf{A} \\ \text{Minimize} \int_{\Gamma} \chi \left(\mathrm{Tr}\left(\delta \check{\mathbf{U}}\right)|_{\Gamma} - \mathrm{Tr}\left(\delta \hat{\mathbf{U}}\right)|_{\Gamma}\right)^2 d\mathbf{A}\end{gathered} \tag{21}$$

In Eq.(21a) $\hat{N}$ is the number of structural mesh nodes, $\check{N}$ is the number of the CFD mesh nodes on the boundary walls, S_i are base functions in the aerodynamic domain surface approximation, h_{ij} is the single term of the interpolation matrix $\mathbf{H}$ and m is the index for the node of CFD mesh. In Eq.(21b) χ is the weight RBF function and Γ is the virtual surface on which the traces of $\delta\hat{\mathbf{U}}$ and $\delta\check{\mathbf{U}}$ are, respectively, projected. For a comprehensive estimation of χ, please refer to [23], [55]. From a computational point of view, the calculation of the RBF requires the definition of the number of points on which the interpolation must be evaluated, the order of the weight functions and the extension of the influence radius. These are all user's input.

The static aeroelastic analysis is provided through a linear staggered iterative process ([36, 37]). First, the aerodynamic loads are calculated on the initial, undeformed configuration at each grid point of the CFD surface mesh. These loads are then converted to loads applied onto the grid points of the structural model through $\mathbf{H}$. The deformed geometry is calculated with those loads, computed around the previous geometry, whether initial or deformed. The conversion can be seen in Eq.(22):

$$\check{\mathbf{U}} = \mathbf{H}\hat{\mathbf{U}} \tag{22}$$

where $\check{\mathbf{U}}$ and $\hat{\mathbf{U}}$ are, respectively, nodal displacements on the fluid mesh and on the structural mesh. It is important mentioning that, being studied with a 2D framework, every structural node will be interested by a load in the loading vector, and the specific coordinate of application is demanded to the f_α term in Eq.(15). Once the structure is deformed, the deformation is mapped back onto the CFD surface mesh using the $\mathbf{H}^T$. Finally, the loads are re-computed on the latest deformed geometry.

The consequent loadings are re-applied on the same undeformed structure ($\mathbf{K}$ is implemented once too), with a consequent new deformed configuration. The displacement fields of these two steps are compared through the mean square error (MSE) [56]. If this error is not under a given tolerance, the process is repeated until the desired inequality between the tolerance and the MSE is reached. The process can be visualized in Fig. 2. An important step in this scheme is the propagation onto the 3D mesh of the discretised volume $\check{\mathbb{V}}$ of the displacements of the structure. To obtain this deformation, a set of linear elastic equations for an elasticity equivalence are employed [57], defining the elastic constants to be used. All features are implemented in `SU2`: the aerodynamic solution for every configuration (deformed and undeformed) is computed running the code `SU2 CFD`, that reads all the inputs given in a configuration .cfg file. The deformation of the 3D CFD domain is obtained through the code `SU2 DEF`, and it requires a configuration file and a text file with the values of displacement for every single boundary mesh node (i.e. the node of the wing); it provides the new deformed 3D mesh as output.

3. Methods validation, calibration and applications

The ~~paper~~ work proceeds with an initial validation and calibration of the disciplinary solvers against available literature data and then presents the application to two test cases. This allows highlighting the potential, flexibility and robustness of the framework herein discussed. The structural ~~solver~~ model is assessed in Section 3.1, whilst the aerodynamic calibration is performed in Section 3.2. The structural test cases are selected to demonstrate the robustness of the combination of CUF, FEM and EPM in representing both the bending and twist of aerodynamic structural

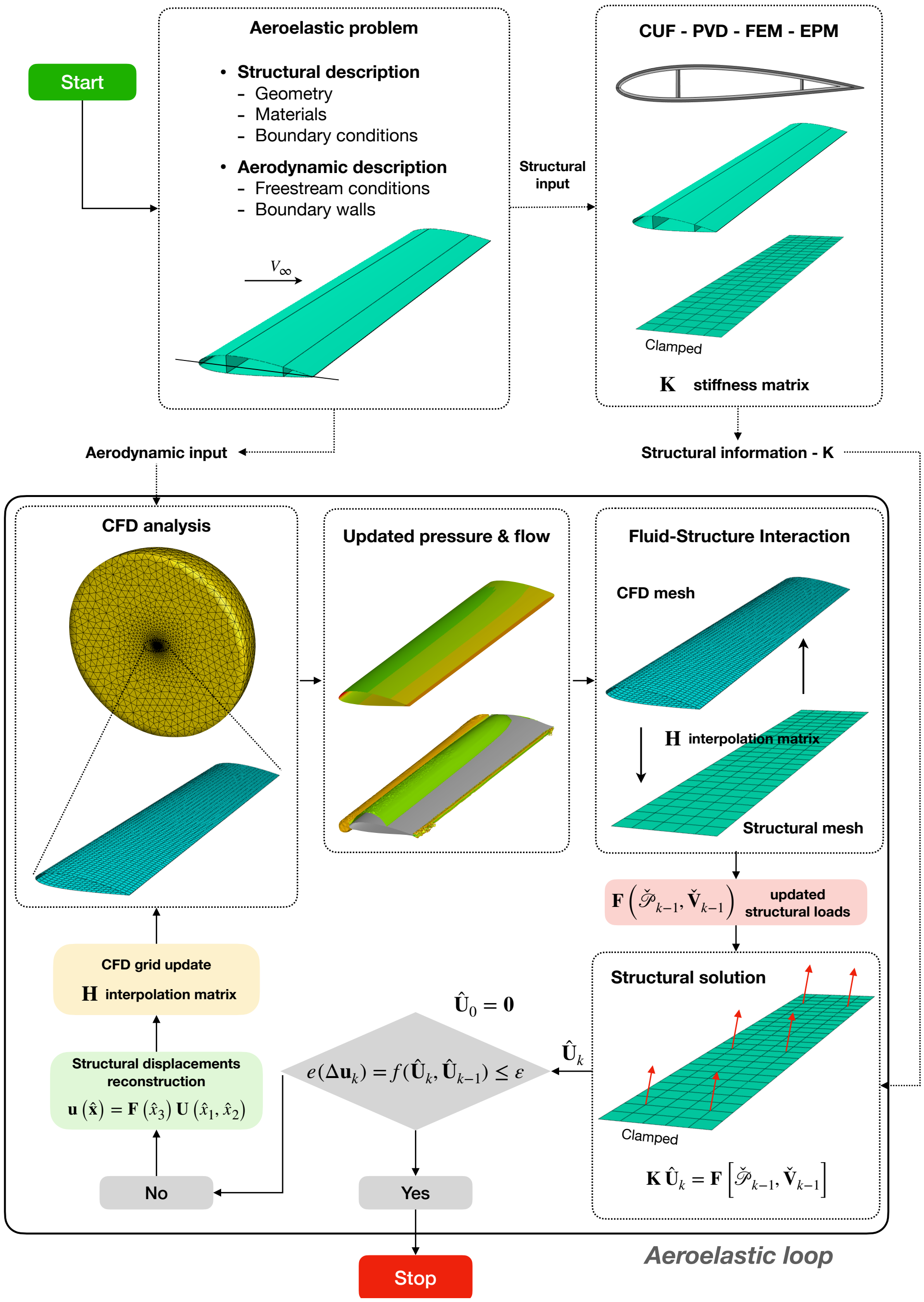

Figure 2: Schematic representation of the developed staggered linear static aeroelastic framework: at each iteration the structural solution provides the input for updating the aerodynamic grid, until convergence between two subsequent solutions is attained.

components, which are crucial for capturing aeroelastic phenomena. The aerodynamic calibration, mainly in terms of mesh convergence within `SU2`, is instrumental to the automation of the staggered iterative procedure presented in Section 3.3- 3.4. The last three sections present applications to various wing configurations. The first is a static aeroelastic analysis of a homogeneous plate subject to an aerodynamic flow in three different low subsonic regimes; the second is a static aeroelastic analysis of an isotropic wing with NACA 2415 airfoil and two spars, subject to a low subsonic aerodynamic regime as well. Both of them confirm the accuracy of the solution against available literature results and also highlighting the potentially problematic presence of phenomena that only high-fidelity aerodynamic tools may capture. Section 3.5 reports several results for the aeroelastic analysis of the same wing, considering the employment of composite laminated material for the wing skin. Overall, the aeroelastic cases are selected to assess the performance of the proposed combination of higher-order CUF/FEM/EPM structural models and high-fidelity CFD; from this point of view, it is worth mentioning that, in the literature, for aeroelastic analysis, CUFs have been employed in conjunction with low-fidelity aerodynamic formulations, e.g. VLM or DLM, but no conjoined use of CUFs and CFD has been reported, to the best of the Authors' knowledge.

In the following, if not otherwise specified, AOA denotes the geometrical angle of attack AOA_g, defined between the aerodynamic chord and the velocity direction. If relevant, this angle is different from the zero-lift angle of attack AOA_{ZL}, defined for any NACA airfoil, and the absolute angle of attack $AOA_a = AOA_g - AOA_{ZL}$, defined between the zero-lift line and the velocity direction.

3.1. Structural model validation

The structural model has been preliminarily assessed for the static analysis of composite laminated plates with different stacking sequences, validating the code implementation and confirming the accuracy of the method.

Figure 3 reports the convergence analysis, with respect to a reference finite element solution, of two laminated plates of size $a \times a \times t$ with $a = 25\,\mathrm{mm}$ and $t = 1\,\mathrm{mm}$, clamped on the four sides and subject to a uniform load $q = 0.01\,\mathrm{N/mm^2}$. Two different stacking sequences are examined, namely $[0/90]_s$ and $[0/75/90]$, and the individual plies exhibit the material properties of graphite-epoxy T300/N5208, as reported in Ref.[58] and summarized in Table 1. Three orders of expansion $N_u = N_{u_1} = N_{u_2} = N_{u_3}$ are considered in the CUF kinematic approximation, see Eq.(1), for the through-the-thickness variation of the displacements and four Gauss points are used for the quadrature of the stiffness contributions. The percentage error $e_{\%}$ is evaluated against `ABAQUS`, considering the maximum plate vertical displacement.

Property	Value
E_1	127.56 GPa
E_2, E_3	13.03 GPa
G_{23}, G_{31}, G_{12}	6.41 GPa
ν_{23}, ν_{31}, ν_{12},	0.3
ρ	1.535×10^{-6}kg/mm^3

Table 1: Material properties for graphite-epoxy T300/N5208 from Ref.[58].

After validating the implementation with composite laminated plates, the use of the model for the analysis of more complex structures of aeronautical interest has been assessed in the framework of higher-order equivalent plate modelling as a tool for aeroelastic analysis. As discussed in Section 2.1, the Equivalent Plate Model is built starting from the kinematic model, applying the PVD and integrating over the thickness of the structure, measured from a reference structural plane over which the fields are interpolated using classical shape functions. The contributions to the discrete structural stiffness matrix are computed by evaluating the fundamental nuclei appearing in Eq.(14) and Eq.(17) where, in case of Taylor-like expansion along the thickness, the integrals along x_3 can be straightforwardly determined analytically. In the procedure, the reference plane x_1x_2 is discretized into finite elements by considering the structural material distribution along x_3, so that regions underlying the external skins of the structure are discretized with different elements with respect to those employed in regions interested by spars and webs.

Several tests have been performed to assess the accuracy and robustness of the developed computational tool. As a benchmark, the results of the static structural analysis of a finite 3D wing are reported and compared against a fully 3D FE benchmark obtained through `ABAQUS`.

The finite wing is the same as that examined in Ref.[59]. It is a rectangular wing with half-wingspan $b = 5\,\mathrm{m}$, NACA 2415 airfoil with chord $c = 1\,\mathrm{m}$; the structure presents two spars at $0.25c$, thickness $t_{s_1} = 0.1h$, and $0.75c$, $t_{s_2} = 0.07h$ and the thickness of the skin is $t_{skin} = 0.04h = 6\,\mathrm{mm}$, where $h = 0.15c$ denotes the height of the airfoil. The skin and the spars are made of a laminated [0/90] composite, with the material properties of the individual plies given in Table 1. A sketch

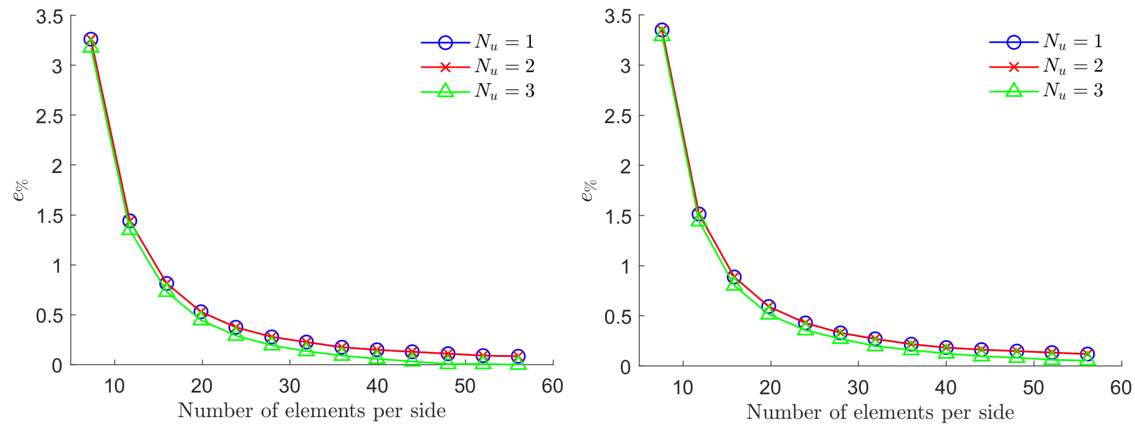

(a) [0/90/90/0]

(b) [0/75/0]

Figure 3: Convergence with respect to reference FE solutions for the linear analysis of composite laminated plates: percentage error $e_{\%}$ *versus* number of elements used in the analysis for the maximum vertical displacement of the plates. Reported results refer to square $a \times a \times t$ plates, with $a = 25\,\mathrm{mm}$ and $t = 1\,\mathrm{mm}$, clamped on the four sides and loaded by a uniform transverse load $q = 0.01\,\mathrm{N/mm^2}$; the lay-ups are *a*) [0/90/90/0] and *b*) [0/75/90] and the individual plies are in graphite-epoxy T300/N5208. The reference solution is computed with `ABAQUS` using (250×250) linear quadrilateral 3D shell elements.

of the transverse section is shown in Fig.(4). The finite wing and the load cases considered for structural validation are shown in Fig.(5a).

A parametric study on the discretization was conducted to examine the influence of the distribution of elements induced by the features of the geometry: for the wing section taken in exam, Fig.(4), the curvature at the leading edge and the presence of the three enclosed regions require a suitable element spacing along the x_1 direction. In other words, the mesh has to be adapted to the geometry. The structural behaviour is assessed by considering separately a bending-dominated and a twist-dominated load case. The validation is done through the comparison with software `ABAQUS` solution, for which a study on the influence of the mesh has been done, up to a very fine configuration of 10^5 shell elements.

The bending-dominated case is provided by applying a uniformly distributed upwards load $q_b = 1\,\mathrm{N/mm^2}$ on the lower surface of the wing, as shown in Fig.(5b). Fig.(6) reports the percentage error $e_{\%}$ related to the computed maximum displacement u_z along the wingspan, recorded at the trailing edge of the tip section of the wing, with respect to the reference FE solution value, computed with `ABAQUS`. It is observed that, in the present case, the order of expansion of the kinematic model

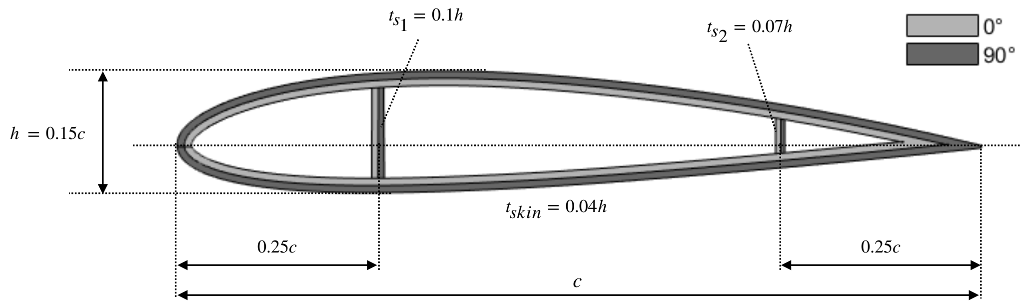

Figure 4: Sketch of the wing transverse section with a NACA 2415 airfoil: $c = 1\,\mathrm{m}$; the $0°$ layer is oriented so that the fibers lay on the drawing plane, while fibers are orthogonal to it for the $90°$ layer.

and the discretization along the wingspan have a higher effect on the convergence with respect to the number of elements along the chord.

A similar parametric study has been conducted for a twist-dominated load case, obtained by loading the wing as shown in Fig.(5c), where $q_t = 100\,\mathrm{N/mm^2}$. Fig.(7) reports the maximum displacement $u_{z,max}$ and the quantity $\Delta u_{z,tip} = u_z(0, b, 0) - u_z(c, b, 0)$, representative of the twist, in terms of percentage error with respect to the FE reference solution; the obtained results, computed using 13 nodes along the chord, show that the twist-dominated case is more sensitive to the order of expansion of the kinematic model with respect to the bending-dominated one, and thus highlights the convenience of higher-order computational tools for the structural analysis of complex load cases.

3.2. Setting Best Practice for CFD

Preliminary studies were carried out to set the best practice to obtain good CFD data, with attention to mesh generation and grid convergence, as the quality of the initial CFD grid is critical to maintain a good grid quality during the iterative process of mesh deformation and warping, Fig.2. The match between the results obtained by the performed computations and some benchmark experimental and computational results was assessed at this stage.

An asymmetric airfoil (NACA 4415) has been analyzed. Navier-Stokes equations with laminar flow hypothesis are used for the CFD simulation. The mesh is generated after a validation made changing the mesh characteristics, so to validate their influence on the results: in particular, different values of farfield extension, in a range between $30c$ and $100c$ (being the aerodynamic chord $c = 1\,\mathrm{m}$),

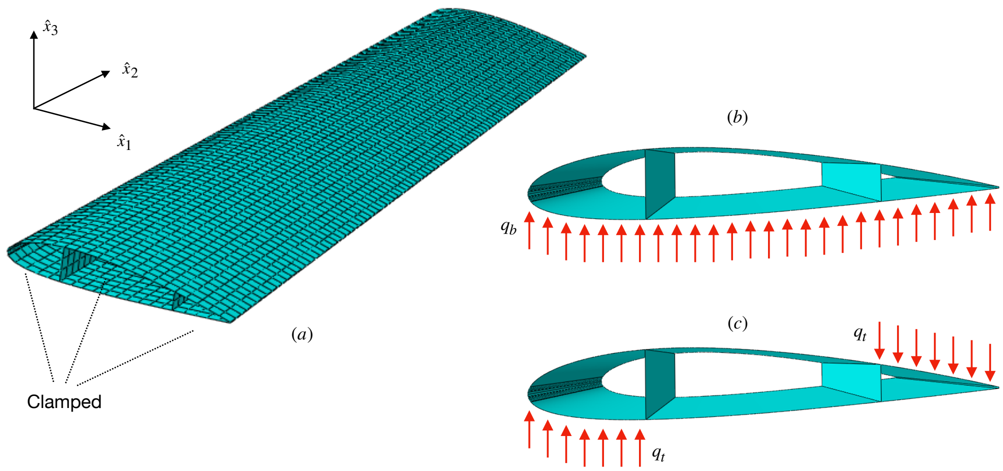

Figure 5: EPM Validation test: a) `ABAQUS` discretization and boundary conditions for the analysed reference wing; b) bending-dominated load case: the distributed load $q_b = 1\,\mathrm{N/mm^2}$ is applied over the lower wing surface and it is aligned with the $\hat{x}_3$ axis; c) torsion-dominated load case: the distributed load $q_t = 100\,\mathrm{N/mm^2}$ is applied over the lower wing surface forward of the first spar, and over the upper wing surface aft of the second spar, and the loads are aligned with the $\hat{x}_3$ axis.

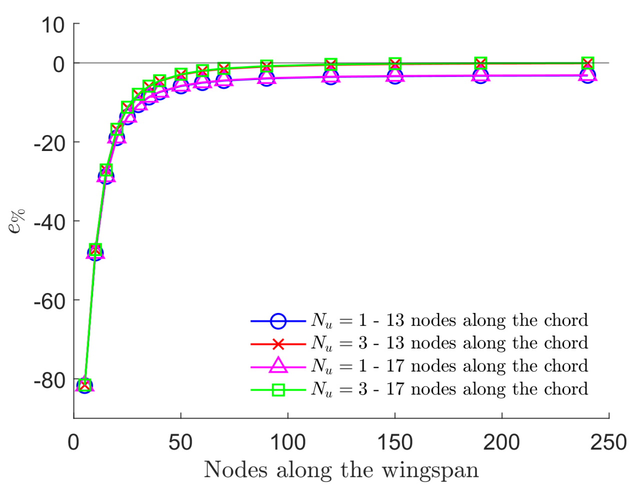

Figure 6: EPM Validation - 13 and 17 nodes along the chord - Convergence studies and validation for bending with composite material from Tab.1. Reference data from `ABAQUS` software: 127500 linear quad elements (approximate global size = 0.01), shell elements.

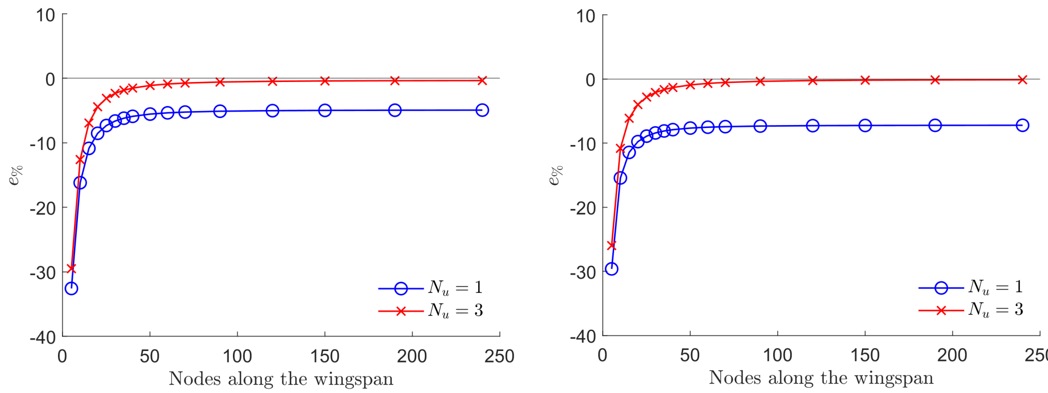

(a) $u_{z,max}$ (b) $\Delta u_{z,tip}$

Figure 7: EPM Validation - 13 nodes along the chord - Convergence studies and validation for torsion with 0/90-laminated material. Reference data from `ABAQUS` software: 127500 linear quad elements (approximate global size = 0.01), shell elements

have been tested, along with three different values of y^+ (0.75, 0.9 and 1). This process has been adopted to observe flow calculations over the two-dimensional NACA 4415 airfoil, studied in a O-type domain. The flow is standard air at sea level, $Re = 10^6$ and $V_\infty = 29.22\,\mathrm{m/s}$. A comparison of the results (C_L and C_D, respectively, the lift coefficient and the drag coefficient, and AOA, the angle of attack) with the ones proposed by [60] is shown in Fig.8. The increase of C_L error can be visualized with the increase of AOA; C_D stays within the range of reference values even with the increase of AOA. The differences between present results and reference, located mainly in the region of critical $AOA = 12°$, can be addressed to the use of a O-type domain instead of a C-type one, as well as to the use of the software `ANSYS FLUENT` for the reference results against the use of `SU2` in the present one, and to the use of structured mesh on the wing surface in the present study against the unstructured mesh of the reference one. Moreover, the present grid employs lower values of y^+ than the ones employed in the reference, where a distribution of y^+ ($\check{x}_1$) between 15 and 40 is adopted. The choices of the present grid properties are made in compatibility with the choices made for the subsequent CFD analysis in the next sections. In both present and reference analysis a fully turbulent flow has been considered. The reference denotes the over-prediction of its CFD $k-\omega$ C_L results with respect to the experimental results, coming from Ohio State University (OSU) [61] and XFOIL software (XFOIL) [62], and it is worth noticing that both OSU and XFOIL give different results; in C_L the under-prediction of present `SU2` results (still in critical AOA region) gives back anyway a lower error than the reference results with respect to OSU values, which are the main benchmark to consider; in C_D comparison, present SA results show a more accurate output than the reference SA one, and OSU reference is well reproduced by present results (both SA and $k-\omega$) at least until the reach of the critical AOA value.

In Fig.9 the extended domain (radius of the farfield $r_f = 100c$, $y^+ = 0.9$) employed for the CFD simulation is visualized. The refinement of the mesh near the leading edge and the traling edge can be easily observed: it is caused by the increase of curvature of the wall, thus the increase in the variation of the fluid dynamics variables. 100 nodes are used for both the upper and lower part of the airfoil, with 48,400 2D elements (triangles, quadrilaterals) in the entire domain.

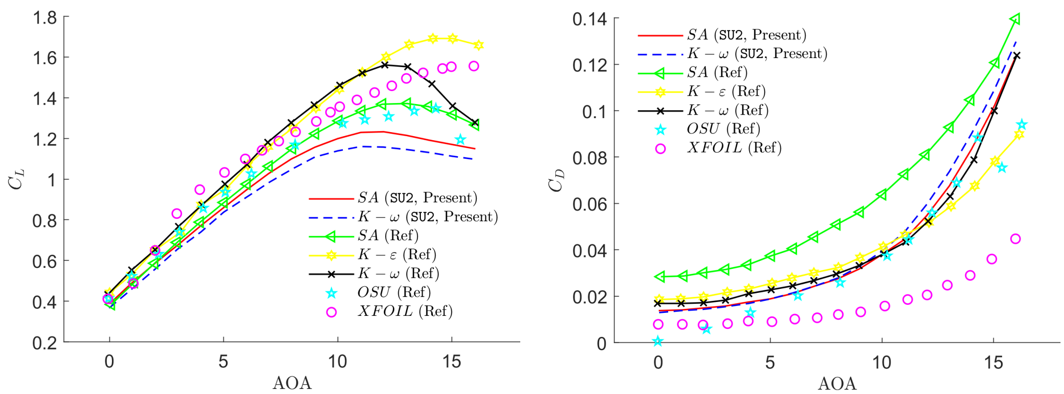

Figure 8: C_L and C_D vs. AOA [°]: present results - SU2 with Spalart-Allmaras and K-ω turbulence models - against Ref.[60] - computational results and experimental (OSU) data - for a NACA 4415 airfoil ($Re = 10^6$, $V_\infty = 29.22\,\mathrm{m/s}$, $r_f = 100c$, $y^+ = 0.9$, 200 linear nodes on the airfoil and 48400 2D elements in the domain)

A further investigation of the CFD tool adopted for this research was conducted on a 3D wing with a NACA 0012 airfoil, subject to a low subsonic freestream. The present results are compared with two benchmarks coming from [63] in terms of C_p profile at the mid-semi-span: experimental data (SAAB FP) and IRPHE CFD analysis. The wing has chord $c = 0.48\,\mathrm{m}$ and span $b = 1.783c$; Reynolds and Mach numbers are, respectively, 10^6 and 0.18; in Fig.10 a comparison between the benchmark CFD results and SU2 results is presented for an angle of attack $AOA = 12°$ at Mach $M_\infty = 0.18$. For the `SU2` results, 80 linear nodes are used on the chord direction, and 150 linear nodes are used in the span direction; after the selection of $y^+ = 0.25$ and $r_f = 50c$, a total of about two million elements (tetrahedrals, hexahedrals, prisms and pyramids) has been reached. The CFD IRPHE results are obtained with a C-type domain of $200 \times 50 \times 50$ 3D elements, obtained from the

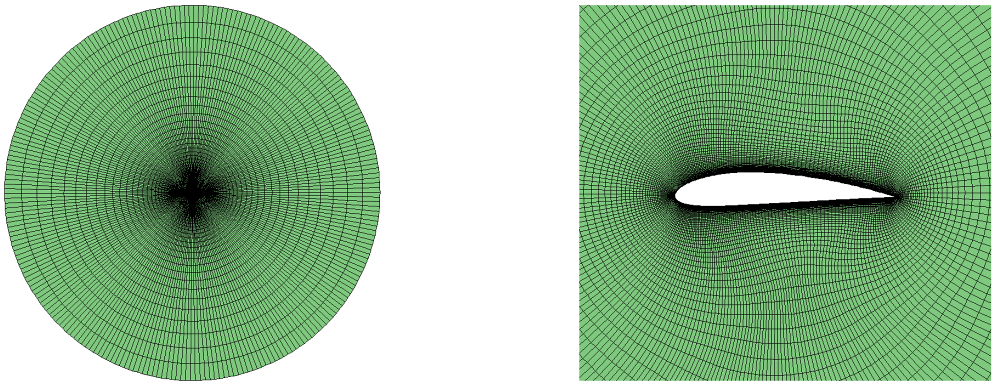

(a) Control Volume 2D (b) Detail of the airfoil

Figure 9: NACA 4415 - CFD 2D domain

extrusion of a C-type 2D domain for a NACA 0012 airfoil analysis, and they confirm the quality of the selected 3D CFD grid.

SU2 outputs show to be in good agreement with the results coming from the reference, in particular with SAAB FP computational results that are used in the reference as benchmark of IRPHE experiments results and employs a full potential solver for the flow.

3.3. Static aeroelastic analysis - Rectangular wing

The first validation test case of a static aeroelastic analysis is performed for a clamped, rectangular Aluminium plate. The plate has a span $b = 5\,\mathrm{m}$, chord $c = 1\,\mathrm{m}$ and thickness $t = 20\,\mathrm{mm}$. The freestream angle of attack is $AOA = 1°$, and three flow velocities, $V_\infty = 10$, 30, and $50\,\mathrm{m/s}$, are considered. In Ref.[59], this configuration was studied employing the VLM [21], the Spline Method [22] and 20 B4 structural mesh elements. The maximum vertical displacement at the leading edge of the tip section was chosen to assess convergence and accuracy of the results. In that work, results were compared to the response provided by NASTRAN sol 144.

Herein, the structural equivalent plate model is combined with the CFD solver [64] through the MLS patch technique. After some preliminary evaluations, a structural 2D mesh comprised of 1,036 in-plane linear elements has been selected. The chosen distribution of elements follow the

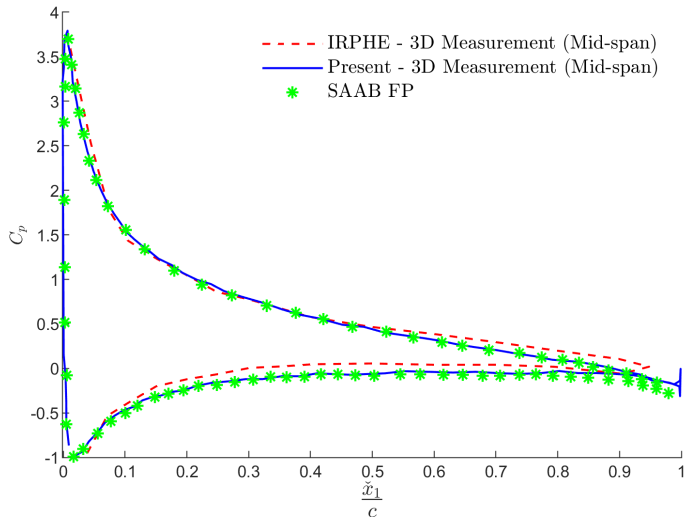

Figure 10: Pressure coefficient C_p distribution around NACA 0012 airfoil (mid-span) at $M_\infty = 0.18$ and $AOA = 12°$; "IRPHE - 3D Measurement (mid-span)": CFD data from Ref. [63], "SAAB FP" computational data coming from Ref. [63], "Present": SU2 data using Spalart-Allmaras equations with laminar flow ($Re = 10^6$, $y^+ = 0.25$, $r_f = 50c$, 80 nodes on the chord direction, 150 nodes on the span direction, 1854555 3D elements in the domain)

consideration given in Section 3.1. Navier-Stokes equations with a laminar hypothesis have been employed for the fluid analysis in `SU2`.

First, some convergence considerations are addressed for the proposed framework. In Ref.[59], the present test is addressed giving some emphasis to the difference between the static structural analysis (SSA), where the aerodynamic loads are computed around the initial, underformed geometry only, and the static aeroelastic analysis (SAA), where the fully coupled fluid-structure interaction procedure is carried out until convergence. In this framework, a staggered iterative approach is employed for computing the SAA, while the SSA is taken at the first step of the staggered procedure. Fig.(11) reports the vertical displacement of the leading edge wing tip. The comparison of the SAA is made against `NASTRAN`, as reported in Ref.[59]. The solution of the SAA was deemed converged when the percent error

$$e\left(\Delta \boldsymbol{u}_k\right) = \left[\frac{\left(\boldsymbol{u}_k - \boldsymbol{u}_{k-1}\right)^{\mathsf{T}}\left(\boldsymbol{u}_k - \boldsymbol{u}_{k-1}\right)}{\boldsymbol{u}_{k-1}^{\mathsf{T}}\boldsymbol{u}_{k-1}}\right]^{\frac{1}{2}}, \tag{23}$$

met the set tolerance of $\varepsilon = 0.001\%$. Here, $\boldsymbol{u}_{k-1}$ and $\boldsymbol{u}_k$ indicate the displacements at two subsequent iterations. The convergence trend changes according to the selected V_∞, decreasing the height of the wave in the evolution with the increase of V_∞. This is likely due to the role of viscosity and its relevance in the CFD results. The evaluation of the comparison with `NASTRAN`, reported in the figure, should keep in account that `NASTRAN` employs FSDT theory for the structural analysis and VLM for the aerodynamic analysis.

The actual deformed configuration for $V_\infty = 50\,\mathrm{m/s}$ and $N_u = N_{u_1} = N_{u_2} = N_{u_3} = 3$ is shown in Fig.(12). The initial geometry is reported in light grey colour, the first iteration of the staggered procedure that is equivalent to SSA is depicted in light green, and the SAA geometry (after 7 iterations) in dark green. Note the displacement is rescaled for plotting purposes.

Fig.(13) shows the evolution of the flow solver for the case $V_\infty = 10\,\mathrm{m/s}$ and $N_u = 3$. At each main iteration of the staggered analysis, the flow solver converges in about 600 inner iterations, setting a convergence tolerance of 10^{-5} and a Courier-Friedrichs-Levy (CFL) number of $CFL = 5$. For validation, accuracy was preferred over time optimization.

In Table 2 the results obtained from the developed approach are compared with those reported in Ref.[59]. With $N_u = 3$, the model provides results in good agreement with those provided by `NASTRAN` for the $V_\infty = 30\,\mathrm{m/s}$ and $50\,\mathrm{m/s}$. However, in the case $V_\infty = 10\,\mathrm{m/s}$ a larger error with respect to the reference solution is found. This is attributed to the viscous effects that are more prominent at the lower velocity test case. The reference `NASTRAN` solution was obtained using DLM, which is an inviscid potential panel method neglecting any viscosity. However, the apparent non-linearity in the flow can be observed in Fig.(14) where the streamlines identified by the components of the skin friction coefficient on the wing surface are drawn. The visible non-linear behaviour, implying the role of viscosity, can not be detected by DLM. Further details about the structure of the flow for the three different freestream velocities are reported in Fig.(15), which shows the value of low pressure in the separation region on the upper surface of the plate, present in all three cases, although less evident for the lower velocity. For $V_\infty = 30\,\mathrm{m/s}$ and $V_\infty = 50\,\mathrm{m/s}$, it is somewhat fortunate to have the VLM provide mediocre predictions, by chance rather than intention as it lacks any mechanism to capture the physics of the flow, most evident at the lowest velocity of $V_\infty = 10\,\mathrm{m/s}$. This example demonstrates how, even for such simple configuration, low-velocity freestream regimes may give rise to non-linear fluid phenomena that may become influential in applications such as energy harvesting through highly-flexible micro wind devices [65], for which the developed framework, suitably extended, could provide a valuable virtual testing tool.

The computational cost required for the analyses is approximately 134 CPU hours for $V_\infty = 10$

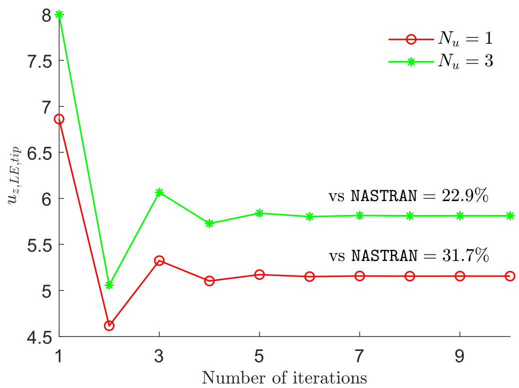

(a) LE tip displacement (mm) for 10 m/s

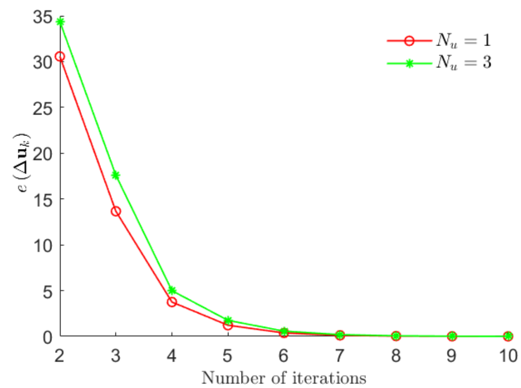

(b) Error for 10 m/s

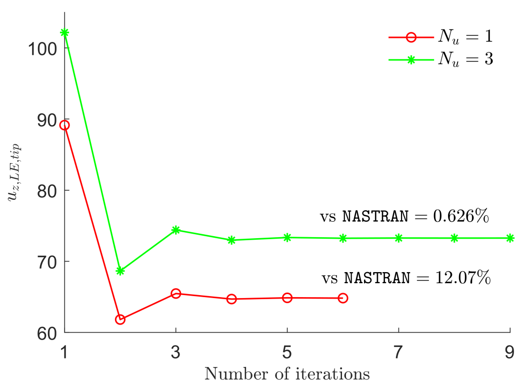

(c) LE tip displacement (mm) for 30 m/s

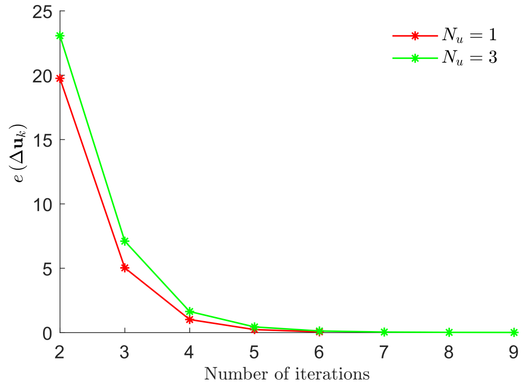

(d) Error for 30 m/s

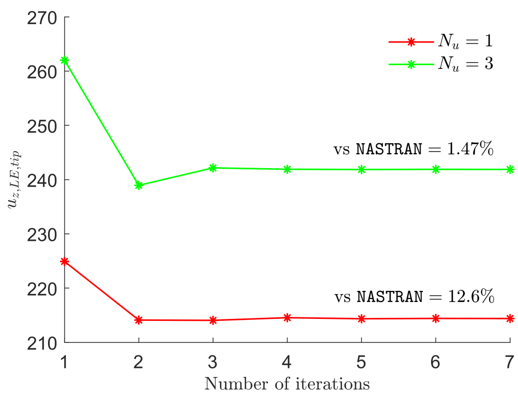

(e) LE tip displacement (mm) for 50 m/s

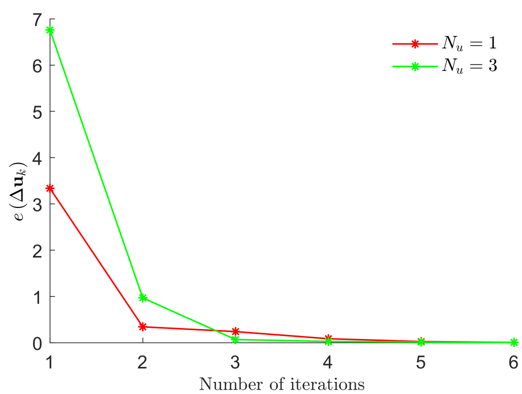

(f) Error for 50 m/s

Figure 11: Rectangular wing - Convergence for displacement (mm) and error in staggered iterative method (Navier-Stokes equations, $AOA = 1°$); percentage comparisons against `NASTRAN` results from [59] are reported

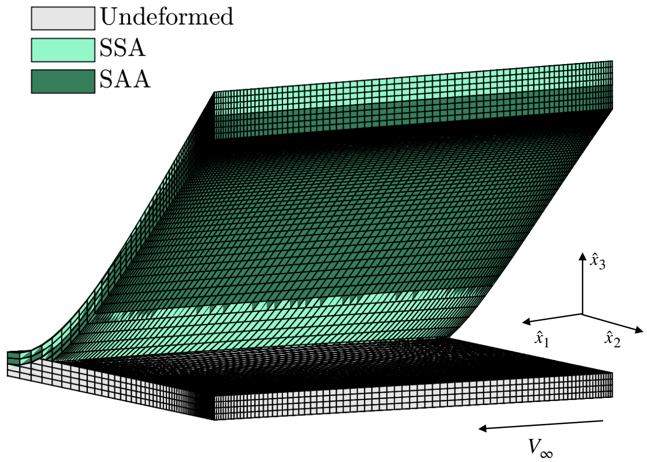

Figure 12: Deformed configurations for the rectangular wing at different staggered steps: the difference between SSA and SAA (7th step) is highlighted with respect to the undeformed configuration. The displacements and the axes proportions are altered for visualization purposes, but it is observed that the difference of maximum displacement between SSA and SAA is of the order of the plate thickness. Data: $b = 5\,\mathrm{m}$, $c = 1\,\mathrm{m}$, $V_\infty = 50\,\mathrm{m/s}$, $N_u = 3$.

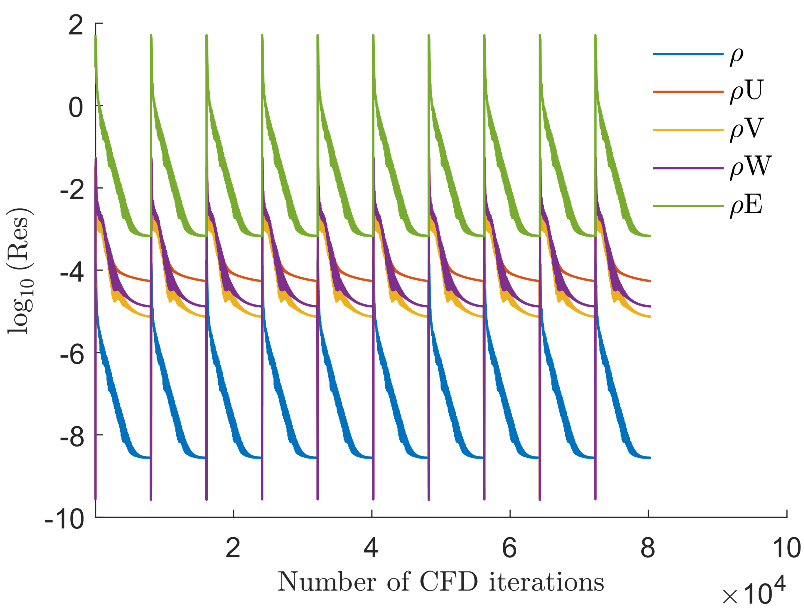

Figure 13: Residuals for the test case $V_\infty = 10\,\mathrm{m/s}$, $N_u = 3$: ρ is the residual on the mass equation; ρU, ρV and ρW are referred to the three directions momentum equations; ρE indicates the residual on the energy equation.

Model N_u	$V = 10\,\mathrm{m/s}$	$V = 30\,\mathrm{m/s}$	$V = 50\,\mathrm{m/s}$
0 - Beam	7.6272	68.611	190.40
1 - Beam	7.6275	68.622	190.48
2 - Beam	7.0244	68.236	190.48
3 - Beam	7.4966	73.241	224.45
4 - Beam	7.5126	73.797	243.94
NASTRAN	7.5446	73.731	245.49
1 - Plate	5.1555	64.828	214.44
3 - Plate	5.8113	73.268	241.90

Table 2: Vertical displacements (SAA) at the tip section LE [mm] for the rectangular wing with $AOA = 1°$. The figure 0 stands for the Euler-Bernoulli beam model, whilst the other figures indicate the used order of expansion N_u; the beam model reference values are taken from Ref.[59], while the plate solutions are those provided by the developed model.

m/s, 318 CPU hours for $V_\infty = 30$ m/s, and 180 CPU hours for $V_\infty = 50$ m/s.

3.4. Static aeroelastic analysis - Wing with NACA 2415 Airfoil

An unswept, untapered and isotropic wing with a NACA 2415 airfoil section is analysed in this Section. The wing has the same planform as that of the rectangular wing previously examined, i.e. wingspan $b = 5\,\mathrm{m}$ and chord $c = 1\,\mathrm{m}$, and its transverse section has the same dimensions as those given in Fig.(4), although in the first application it is studied as isotropic and not laminated. The same configuration has also been analysed in Ref.[59], which is used as benchmark. The wing is subject to a freestream velocity with $V_\infty = 50\,\mathrm{m/s}$ with an absolute angle of attack $AOA_a = 3°$, corresponding to a geometric angle of attack $AOA_g = 0.98°$ (CFD zero-lift angle $AOA_{ZL} = -2.02°$). The CFD analysis is performed adopting SA turbulence model. The fluid-structure coupling strategies are the same as those previously discussed. About 280 CPU hours were needed for computing a converged solution.

Fig.(16) reports the convergence of the displacement of the tip section leading edge and of the quantity $e\left(\Delta \boldsymbol{u}_k\right)$, Eq.(23), for $N_u = 1$ and $N_u = 3$. In Fig. 17 the evolution of the residuals on the different CFD variables is reported.

Differently from what has been observed for the rectangular wing, the employment of the airfoil,

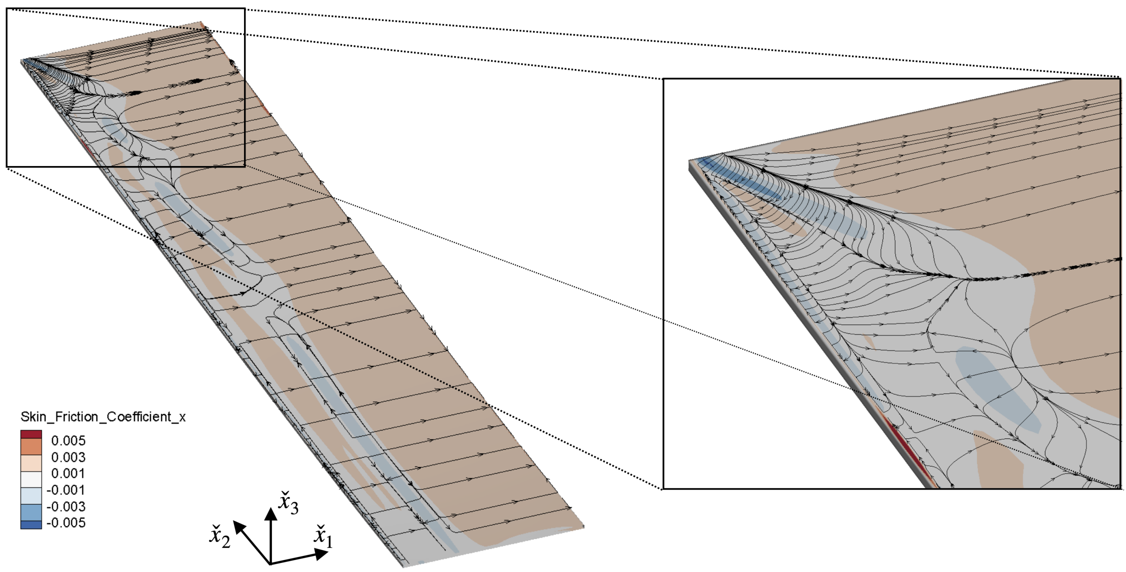

Figure 14: Skin friction coefficient patch and streamlines near leading edge in proximity of the tip section for the SSA response; Rectangular wing, $V_\infty = 50\,\mathrm{m/s}$, $AOA = 0.98°$.

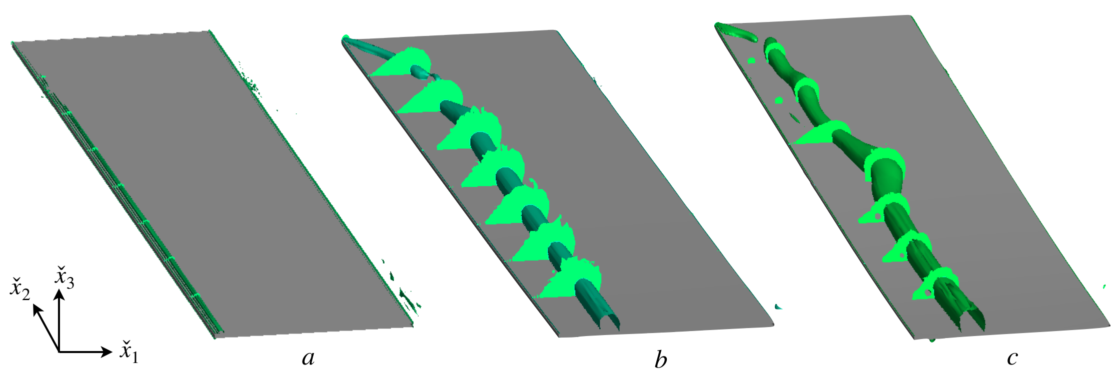

Figure 15: 3D patch of the low pressure region, with selected values of pressure p, with $N_u = 3$: a) $V_\infty = 10\,\mathrm{m/s}$, $p = 101\,294\,\mathrm{Pa}$; b) $V_\infty = 30\,\mathrm{m/s}$, $p = 100\,997\,\mathrm{Pa}$; c) $V_\infty = 50\,\mathrm{m/s}$, $p = 100\,553\,\mathrm{Pa}$. The reported configurations are those computed for the SAA, as can be noted e.g. from the deformation in the case (c).

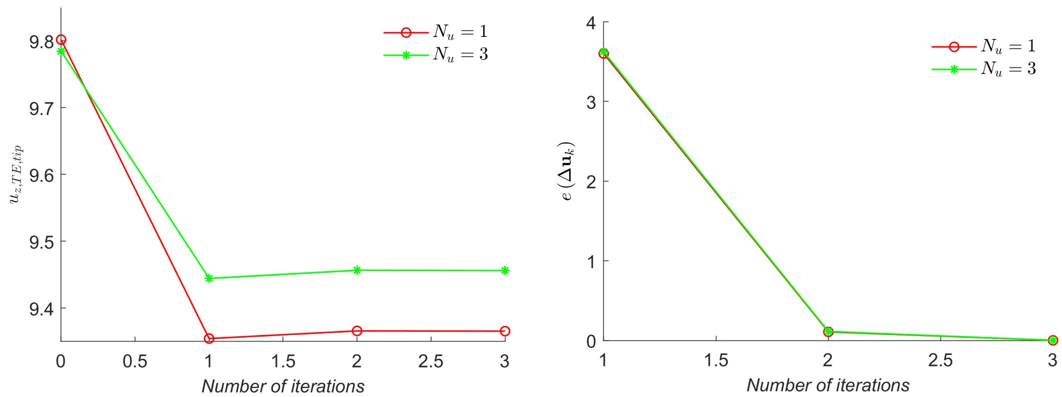

Figure 16: Convergence for maximum displacement [mm] and error in staggered iterative method for wing with NACA 2415 airfoil ($V_\infty = 50\,\mathrm{m/s}$, $N_u = 1, 3$, $AOA = 0.98°$).

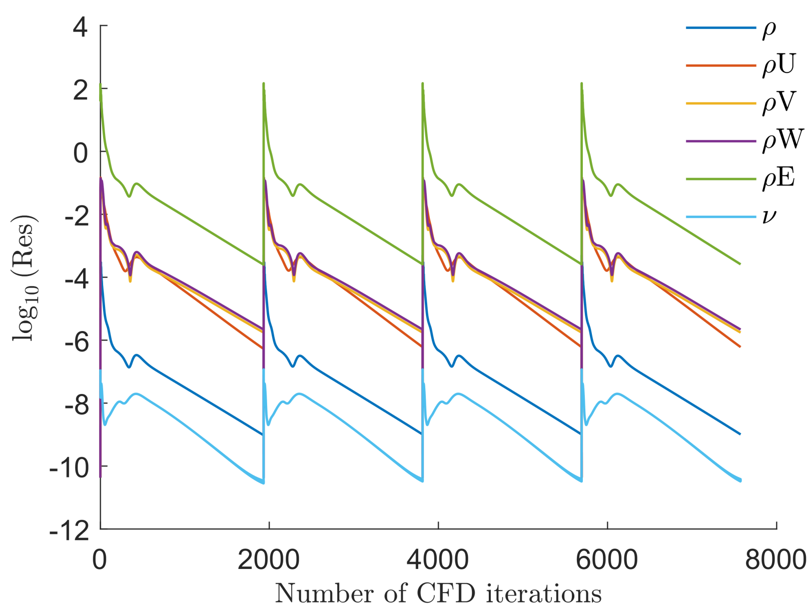

Figure 17: Residuals for the wing NACA 2415 test case $V_\infty = 50\,\mathrm{m/s}$ $N_u = 3$; ρ is the residual on the mass equation; ρU, ρV and ρW are referred to the three directions momentum equations; ρE indicates the residual on the energy equation; ν indicates the residual on the viscosity term.

in the mentioned aerodynamic regimes, prevents flow separation; the absence of relevant non-linear phenomena thus promotes a quicker convergence of the overall scheme. The maximum displacement is located at the trailing edge of the tip section, as in [59], due to the combination of wing twist and bending. The increase of the order of expansion N_u of the structural model leads to a more accurate description of the torsion at the tip. However, with $N_u = 3$, the reference point displacement converges to 9.46 mm versus the value 8.84 mm reported in Ref.[59]: the 7% difference is likely due to the difference between the aerodynamic models employed in the two cases, capturing different physics of the flow; in particular, it has been observed that, in the performed tests, CFD and VLM provide two different estimates of the zero-lift angle of attack for the overall wing. Fig.(18a) reports the distribution of the iso-surfaces for two pre-selected C_p values, which thus identify regions of low and high pressure; in Fig.(18b) the $\check{x}_1$-velocity streamlines are shown, in confirmation of the overall linear behavior of the fluid for this wing test case.

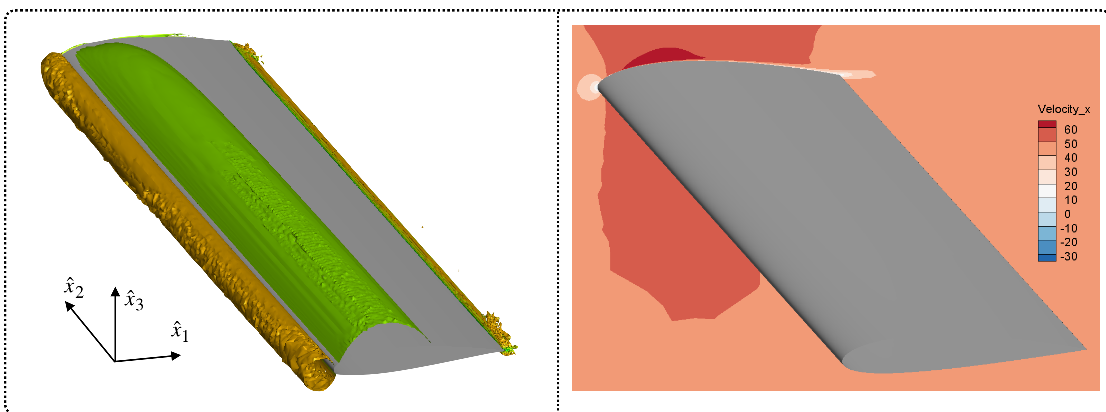

(*a*) (*b*)

Figure 18: Rectangular wing with NACA 2415 airfoil, $b = 5\,\text{m}$, $c = 1\,\text{m}$, $V_\infty = 50\,\text{m/s}$, $N_u = 3$, $AOA = 0.98°$: (a) Isosurfaces for pressure coefficient values $C_p = 0.19$ and $C_p = -0.38$ in the SAA CFD simulation; (b) Visualization of $\check{x}_1$-velocity streamlines for the SAA CFD simulation.

3.5. Preliminary aeroelastic tailoring of a composite wing with a NACA 2415 airfoil

The developed framework can be employed to investigate the effect of the structural layout on the aeroelastic response. In this section, analogously to what done in Ref.[59], upon adopting a composite configuration, the effect of the fibers orientation on the aeroelastic response of the NACA 2415 wing is analysed. The geometry of the wing is the same as that considered in the previous section, while the skin and spars are comprised by a single composite layer whose orientation is varied in the different analyses. The composite material properties are reported in Table 3.

Property	Value
E_1	20.5 GPa
E_2, E_3	10 GPa
G_{23}, G_{31}, G_{12}	5 GPa
ν_{23}, ν_{31}, ν_{12},	0.25

Table 3: Material properties for the single-layer composite material as from Ref.[59].

The fiber orientation is defined with respect to the freestream direction, so that $\pm 90°$ identify fibers directed along the wingspan, see Fig.(19). Moreover, it is important to note that the fiber orientation is defined independently for the top and bottom wing surfaces; in other words, the wing skin is not obtained by folding a single composite layer, but two layers with the same fiber orientation are employed for them. In this way, $45°$ in the geometry from Fig.(19) describes the case in which the fibers travel from the leading to the trailing edge getting progressively further from the root section and closer to the tip section, for both the lower and upper wing surfaces; if the skin were obtained by folding a single composite sheet, when the upper surface fibers would have a $45°$ orientation, the lower surface fibers would be oriented as $-45°$. The fiber orientation over the spars is described considering them as an upper surface region with the normal directed along the freestream direction.

The results are reported in terms of maximum vertical displacement at the tip wing section and in terms of tip section twist versus fibers orientation angle in Fig.(20) and versus freestream velocity in Fig.(21).

The description adopted for the fiber orientation explains the π-periodic distribution of the results observed in Fig.(20). It is worth mentioning that the 3D CFD mesh employed for the flow solution under varying freestream conditions is adapted according to the velocity in Fig.(21).

The preliminary aeroelastic tailoring suggests that a trade-off should be made between the configuration that minimises the tip displacement, $-40°$, and that minimising the wing twist,

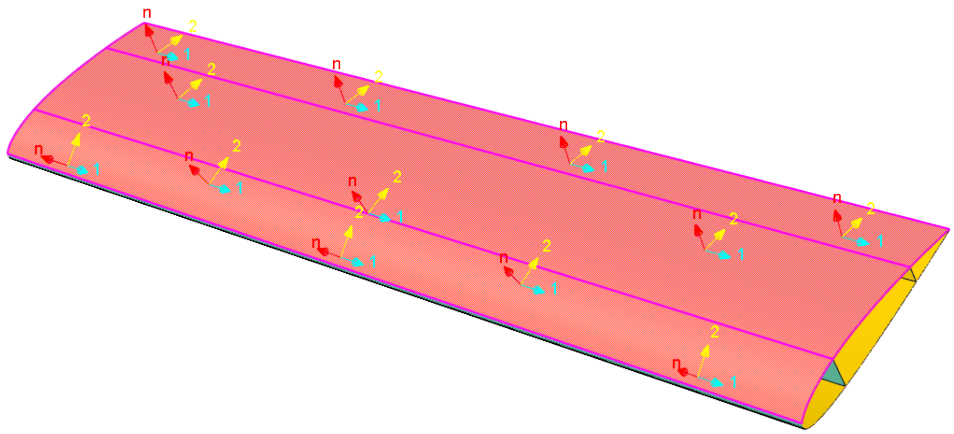

Figure 19: Schematic orientation of the fibers over the upper wing surface: the fibers are directed along the 1-axis and, the depicted case corresponds to $-90°$.

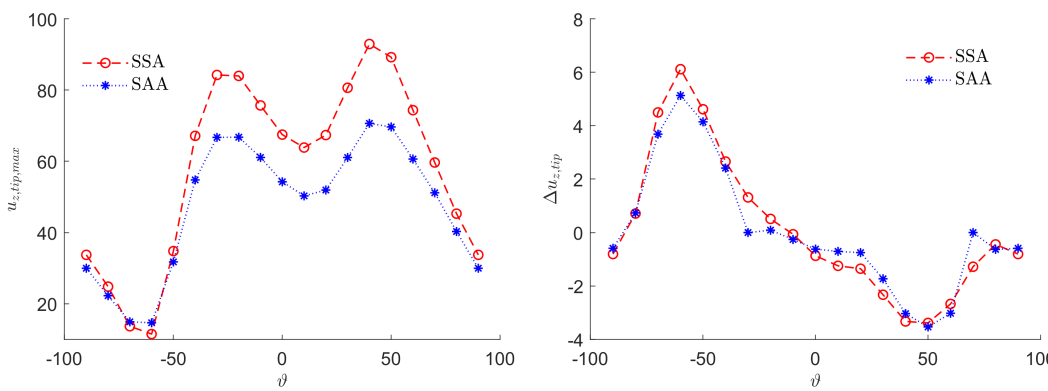

Figure 20: Vertical tip displacement (mm) and tip section twist (mm) for the NACA 2415 wing vs. the angle ply orientation [°]. a) $u_{z,tip,max}$; b) $\Delta u_{z,tip}$ ($V_\infty = 50\,\mathrm{m/s}$, $N_u = 3$, $AOA = 0.98°$, RANS SA equations)

$-10°$, if the absolute value is considered. The study solves an optimization problem with respect to the fiber orientation. It is found that the wing twist is one order of magnitude lower than the displacement. This motivated our selection of the $\pm 90°$ fiber orientation for the analysis reported in Fig.(21), where the differences between SSA and SAA solutions for increasing values of freestream velocity are illustrated.

The proposed CFD-based method does not allow a direct calculation of the divergence velocity, which is a drawback; however, this is counterbalanced by the possibility of assessing higher velocity

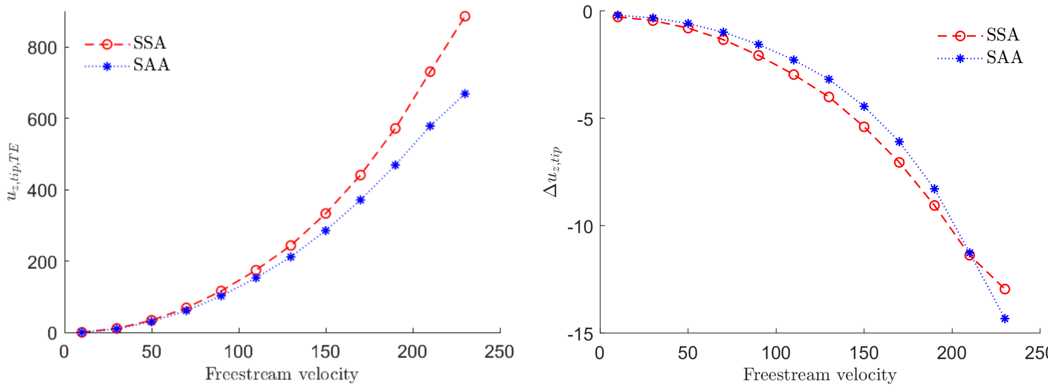

Figure 21: Vertical tip displacement (mm) and tip section twist (mm) for the NACA 2415 wing vs. the freestream velocity (m/s). $\pm 90°$ single ply angle. a) $u_{z,tip,max}$; b) $\Delta u_{z,tip}$ ($N_u = 3$, $AOA = 0.98°$, RANS SA equations)

regimes, as shown in Fig.(21), where the wing response is shown for Mach numbers in the range $M_\infty = 0.03$ to $M_\infty = 0.67$. The developed tool can be used also to investigate the transonic regime.

4. Discussion and further developments

Results herein presented show the potential of the developed CUF/FEM/EPM/CFD framework. The unique contribution of this work is the implementation of a static aeroelastic framework based on a high-order representation for the structure, based on CUF/FEM/EPM, and high-fidelity for the aerodynamics, based on CFD. This work goes beyond the state-of-the-art in CUF/EPM, generally coupled with potential flow solvers. Indeed, the model couples a variable-order structural formulation with a high-fidelity CFD solver, thus allowing the possibility of seamlessly analysing complex non-linear fluid regimes, e.g. either very low-speed cases dominated by viscosity effects or high-subsonic and transonic regimes where the effects of compressibility play an important role. The use of the CUF structural formulation, of the open-source flow solver `SU2` and the fluid-structure Python interface allow appreciable flexibility in terms of structural theories, fluid dynamics governing equations, and fluid-structure coupling rules to be embedded. Featuring more advanced disciplinary tools than traditionally employed in an aeroelastic analysis, the current framework may incorporate the physical representation of higher-order structural responses, and viscosity and compressibility effects in the fluid response. The former is relevant for the analysis of complex geometry/material distributions, while the latter provides a single physical interpretation of both low and high flight speeds.

Several aspects deserve some additional considerations, which also identify directions of further investigation. In its current implementation, the framework addresses the *static aeroelastic response* of structures undergoing *small deformations*.

First, the model could be extended to address large-strains kinematics: indeed, CUF has been successfully employed for implementing refined geometrically non-linear plate theories and investigating large-deflection bending and post-buckling response of homogeneous and laminated plates under different boundary conditions [66, 67]. The main difference compared to the current implementation is the updating of the stiffness matrix within the aeroelastic loop, due to the dependence of the geometrically non-linear terms on the deformation. Endowing the framework with such capability will make it suitable for investigating the static aeroelastic response of highly-flexible structural components typical of MALE/HALE aircraft [68].

Another interesting development involves the implementation of a *dynamic* aeroelastic analysis capability: from this point of view, being the use of CUF for structural dynamics already successfully demonstrated [69, 70], the main source of computational costs lie in the CFD run. To overcome the large computational costs associated with time marching the underlying equations, reduced order models for the fluid are a promising alternative. There is a plethora of different techniques, generally classified in data-driven and equations-based methods [71]. The availability of an open-source high-order structural model coupled with a ROM high-fidelity CFD solver for dynamic aeroelastic analysis of flexible structures, able to address both homogeneous and laminated configurations, would provide a tool useful not only for aerospace applications but also for the analysis and design of other applications that are attracting increasing interest, such as energy harvesting from fluid-structure interaction [72, 73]. Dynamic aeroelastic analysis requires nested iterations within the multi-disciplinary analysis tool, so that the coupled system can converge at each time step. This would cause an important increase in the computational burden.

The framework has not been employed for the prediction of static divergence. The static divergence speed could indeed be identified by analysing the incremental response of the structure to increasing freestream velocity, until a loss of solution convergence would numerically signal the attainment of a critical condition. A more effective procedure would require the extraction of the aeroelastic coupling matrix from the flow solver `SU2`, which is not immediate but identifies an interesting direction for further development.

5. Conclusions

A CUF/FEM/EPM/CFD framework was developed, implemented and applied to several static aeroelastic problems using composite structures. The use of a CUF generalized kinematic model allows the adoption of structural theories of different orders. The structural model was coupled with the CFD open-source aerodynamic solver `SU2` via a dedicated fluid-structure algorithm. The validation of each disciplinary solver of the framework was discussed and results compared to those available in the literature, provided by potential-based aerodynamic formulations. A plate, a homogeneous wing with a NACA 2415 airfoil cross section and a composite wing with the same airfoil were the test cases. Results showed good agreement with reference medium freestream velocities, whilst expected departures are recorded for either very low-speed or high subsonic regimes, signalling and justifying the use of high-fidelity aerodynamics for such cases. Directions of further research for the development of a flexible tool for seamless aeroelastic analysis of a variety structural configurations and aerodynamic regimes are eventually identified and briefly discussed.

Acknowledgements

IB and ADR acknowledge the support of the Department of Engineering of the University of Palermo through the grant *Premio gruppo di ricerca 2020*.

The Authors acknowledge the support of the computational resources of `IRIDIS` at the University of Southampton, UK.

References

[1] L. Wang, X. Liu, A. Kolios, State of the art in the aeroelasticity of wind turbine blades: Aeroelastic modelling, Renewable and Sustainable Energy Reviews 64 (2016) 195–210. doi:https://doi.org/10.1016/j.rser.2016.06.007.
URL https://www.sciencedirect.com/science/article/pii/S1364032116302234

[2] P. Teixeira, C. Cesnik, Propeller influence on the aeroelastic stability of high altitude long endurance aircraft, The Aeronautical Journal 124 (1275) (2020) 703–730. doi:10.1017/aer.2019.165.

[3] S. Brusco, G. Solari, Transient aeroelasticity of structures subjected to thunderstorm outflows, Engineering Structures 245 (2021) 112801. doi:https://doi.org/10.1016/j.engstruct.2021.112801.
URL https://www.sciencedirect.com/science/article/pii/S0141029621009512

[4] D. D. Bueno, L. D. Wayhs-Lopes, E. H. Dowell, Control-surface structural nonlinearities in aeroelasticity: A state of the art review, AIAA Journal 60 (6) (2022) 3364–3376. arXiv:https://doi.org/10.2514/1.J060714, doi:10.2514/1.J060714.
URL https://doi.org/10.2514/1.J060714

[5] Y. Fung, An Introduction to the Theory of Aeroelasticity, Dover Books on Aeronautical Engineering, Dover Publications, 2008.
URL https://books.google.co.uk/books?id=nic3DwAAQBAJ

[6] E. Dowell, E. Crawley, H. Curtiss, D. Peters, R. Scanlan, F. Sisto, A Modern Course in Aeroelasticity, Mechanics: Dynamical Systems Series, Springer Netherlands, 1995.
URL https://books.google.co.uk/books?id=6v5TAAAAMAAJ

[7] D. H. Hodges, G. A. Pierce, Introduction to Structural Dynamics and Aeroelasticity, 2nd Edition, Cambridge Aerospace Series, Cambridge University Press, 2011. doi:10.1017/CBO9780511997112.

[8] R. Jones, Mechanics Of Composite Materials, 500 Tips, Taylor & Francis, 1998.
URL https://books.google.co.uk/books?id=oMph2kNG3yAC

[9] H. Ahmad, A. Tariq, A. Shahzad, M. Faheem, M. Shafiq, I. Abdul Rashid, A. Afzal, A. Munir, M. Riaz, H. Haider, M. A. Afzal, M. B. Qadir, Z. Khaliq, Methods and composite materials—a review, Polymer Composites (2019) 1–16doi:10.1002/pc.25311.

[10] M. H. Shirk, T. J. Hertz, T. A. Weisshaar, Aeroelastic tailoring - theory, practice, and promise, Journal of Aircraft 23 (1986) 6–18.

[11] M. Bordogna, P. Lancelot, D. Bettebghor, R. De Breuker, Static and dynamic aeroelastic tailoring with composite blending and manoeuvre load alleviation, Structural and Multidisciplinary Optimization 61 (5) (2020) 2193–2216. doi:10.1007/s00158-019-02446-w.

[12] O. Stodieck, J. E. Cooper, P. M. Weaver, P. Kealy, Optimization of tow-steered composite wing laminates for aeroelastic tailoring, AIAA Journal 53 (8) (2015) 2203–2215. arXiv:https://doi.org/10.2514/1.J053599, doi:10.2514/1.J053599.
URL https://doi.org/10.2514/1.J053599

[13] B. Zhang, K. Chen, L. Zu, Aeroelastic tailoring method of tow-steered composite wing using matrix perturbation theory, Composite Structures 234 (2020) 111696. doi:https://doi.org/10.1016/j.compstruct.2019.111696.
URL https://www.sciencedirect.com/science/article/pii/S0263822319340231

[14] J. Reddy, Mechanics of Laminated Composite Plates and Shells: Theory and Analysis, Second Edition, CRC Press, 2003.
URL https://books.google.co.uk/books?id=eeUr_AJiGRcC

[15] A. Varello, L. Demasi, E. Carrera, G. Giunta, An improved beam formulation for aeroelastic applications, Collection of Technical Papers - AIAA/ASME/ASCE/AHS/ASC Structures, Structural Dynamics and Materials Conferencedoi:10.2514/6.2010-3032.

[16] R. Vepa, Aeroelastic analysis of wing structures using equivalent plate models, AIAA Journal 46 (5) (2008) 1216–1225. arXiv:https://doi.org/10.2514/1.34928, doi:10.2514/1.34928.
URL https://doi.org/10.2514/1.34928

[17] O. C. Zienkiewicz, R. L. Taylor, J. Z. Zhu, The Finite Element Method: Its Basis and Fundamentals, Sixth Edition, 6th Edition, Butterworth-Heinemann, 2005.

[18] E. Carrera, M. Cinefra, M. Petrolo, E. Zappino, Finite Element Analysis of Structures through Unified Formulation, Wiley, 2014.

[19] A. Varello, M. Petrolo, E. Carrera, A refined 1d fe model for the application to aeroelasticity of composite wings, International Center for Numerical Methods in Engineering (CIMNE), Barcelona, Spain, 2011, p. 12.

[20] R. Kapania, Y. Liu, Static and vibration analysis of general wing structures using equivalent plate models, in: 41st AIAA/ASME/ASCE/AHS/ASC Structures, Structural Dynamics and Materials Conference, 2000. doi:10.2514/6.2000-1434.

[21] J. Katz, A. Plotkin, Low-Speed Aerodynamics, 2nd Edition, Cambridge University Press, 2001. URL http://books.google.fr/books?id=rAS1DmBRLo8C

[22] R. L. Harder, R. N. Desmarais, Interpolation using surface splines., Journal of Aircraft 9 (1972) 189–191. doi:10.2514/3.44330.

[23] G. Quaranta, P. Masarati, P. Mantegazza, A conservative mesh-free approach for fluid-structure interface problems, in: Int. Conf. on Computational Methods for Coupled Problems in Science and Engineering COUPLED PROBLEMS 2005, 2005.

[24] A. Varello, E. Carrera, L. Demasi, Vortex lattice method coupled with advanced one-dimensional structural models, Journal of Aeroelasticity and Structural Dynamics 2 (2011) 53–78. doi:10.3293/asdj.2011.10.

[25] M. Petrolo, E. Carrera, L. Demasi, An advanced unified aeroelastic formulation based on 1d higher-order finite elements, in: 15th International Forum on Aeroelasticity and Structural Dynamics 2011 - IFASD2011, 2011.

[26] A. Varello, A. Lamberti, E. Carrera, Static aeroelastic response of wing-structures accounting for in-plane cross-section deformation, International Journal of Aeronautical and Space Sciences 14 (2013) 310–323. doi:10.5139/IJASS.2013.14.4.310.

[27] M. Petrolo, Flutter analysis of composite lifting surfaces by the 1d carrera unified formulation and the doublet lattice method, Composite Structures 95 (Complete) (2013) 539–546. doi:10.1016/j.compstruct.2012.06.021.

[28] A. Pagani, A. de Miguel, M. Petrolo, E. Carrera, Analysis of laminated beams via unified formulation and legendre polynomial expansions, Composite Structures 156. doi:10.1016/j.compstruct.2016.01.095.

[29] L. Demasi, E. Livne, Structural ritz-based simple-polynomial nonlinear equivalent plate approach: An assessment, Journal of Aircraft - J AIRCRAFT 43 (2006) 1685–1697. doi:10.2514/1.17466.

[30] L. Demasi, E. Livne, Aeroelasticity of structurally nonlinear lifting surfaces using linear modally reduced aerodynamic generalized forces, Aiaa Journal - AIAA J 47 (2009) 71–90. doi:10.2514/1.34797.

[31] Y. Yang, Z. Wu, C. Yang, Equivalent plate modeling for complex wing configurations, Procedia Engineering 31 (2012) 409–415, international Conference on Advances in Computational Modeling and Simulation. doi:https://doi.org/10.1016/j.proeng.2012.01.1044.
URL https://www.sciencedirect.com/science/article/pii/S1877705812010685

[32] E. Kim, J.-H. Roh, S.-J. Yoo, I. Lee, Equivalent plate modeling of the wing-box structure with control surface, International Journal of Aeronautical and Space Sciences 7. doi:10.5139/IJASS.2006.7.2.104.

[33] C. Scarth, J. E. Cooper, Reliability-based aeroelastic design of composite plate wings using a stability margin, Struct. Multidiscip. Optim. 57 (4) (2018) 1695–1709. doi:10.1007/s00158-017-1838-6.
URL https://doi.org/10.1007/s00158-017-1838-6

[34] A. Kafkas, G. Lampeas, Static aeroelasticity using high fidelity aerodynamics in a staggered coupled and rom scheme, Aerospace 7 (11). doi:10.3390/aerospace7110164.
URL https://www.mdpi.com/2226-4310/7/11/164

[35] A. D. Ronch, J. Drofelnik, M. van Rooij, J. Kok, M. Panzeri, A. Voss, Aerodynamic and aeroelastic uncertainty quantification of nato sto avt-251 unmanned combat aerial vehicle, Aerospace Science and Technology 91 (2019) 627–639.
URL https://eprints.soton.ac.uk/432379/

[36] L. Yang, C. Xie, C. Yang, Geometrically exact vortex lattice and panel methods in static aeroelasticity of very flexible wing, Proceedings of the Institution of Mechanical Engineers, Part G: Journal of Aerospace Engineering 234 (2019) 095441001988523. doi:10.1177/0954410019885238.

[37] Y. S. Jung, D. Yu, O. Kwon, Aeroelastic analysis of high-aspect-ratio wings using a coupled cfd-csd method, TRANSACTIONS OF THE JAPAN SOCIETY FOR AERONAUTICAL AND SPACE SCIENCES 59 (2016) 123–133. doi:10.2322/tjsass.59.123.

[38] T. D. Economon, F. Palacios, S. R. Copeland, T. W. Lukaczyk, J. J. Alonso, Su2: An open-source suite for multiphysics simulation and design, AIAA Journal 54 (3) (2016) 828–846. arXiv:https://doi.org/10.2514/1.J053813, doi:10.2514/1.J053813.
URL https://doi.org/10.2514/1.J053813

[39] A. O. Nuhait, D. T. Mook, Aeroelastic behavior of flat plates moving near the ground, Journal of Aircraft 47 (2) (2010) 464–474. arXiv:https://doi.org/10.2514/1.41186, doi:10.2514/1.41186.
URL https://doi.org/10.2514/1.41186

[40] M. Filippi, E. Carrera, Aerodynamic and mechanical hierarchical aeroelastic analysis of composite wings, Mechanics of Advanced Materials and Structures 23 (2015) 1–31. doi:10.1080/15376494.2015.1121561.

[41] E. Reissner, The effect of transverse shear deformation on the bending of elastic plates, ASME J. Appl. Mech 12 (1945) 68–77.

[42] R. D. Mindlin, Influence of rotatory inertia and shear on flexural motions of isotropic, elastic plates, Journal of Applied Mechanics 18 (1) (1951) 31–38. arXiv:https://asmedigitalcollection.asme.org/appliedmechanics/article-pdf/18/1/31/6747060/31_1.pdf, doi:10.1115/1.4010217.
URL https://doi.org/10.1115/1.4010217

[43] H. Abramovich, R. Wagner, C. Hühne, S. Niemann, S. Castro, Stability and Vibrations of Thin Walled Composite Structures, 2017.

[44] M. Petrolo, Advanced aeroelastic models for the analysis of lifting surfaces made of composite materials - PhD Dissertation, Politecnico di Torino, 2011.

[45] S. Doll, R. Hauptmann, K. Schweizerhof, C. Freischläger, Selective reduced integration and volumetric locking in finite deformation elastoviscoplasticity.

[46] Y.-H. Na, S. Shin, Equivalent-plate analysis for a composite wing with a control surface, Journal of Aircraft 50 (3) (2013) 853–862. arXiv:https://doi.org/10.2514/1.C032020, doi:10.2514/1.C032020.
URL https://doi.org/10.2514/1.C032020

[47] T. Von Kármán, Mechanische Ähnlichkeit und Turbulenz, Sonderdrucke aus den Nachrichten von der Gesellschaft der Wissenschaften zu Göttingen : Mathematisch-physische Klasse, Weidmannsche Buchh., 1930.
URL https://books.google.co.uk/books?id=GNvQGwAACAAJ

[48] F. Götten, D. Finger, M. Marino, C. Bil, M. Havermann, C. Braun, A review of guidelines and best practices for subsonic aerodynamic simulations using rans cfd, 2019.

[49] T. D. Economon, F. Palacios, S. R. Copeland, T. Lukaczyk, J. J. Alonso, Su 2 : An open-source suite for multiphysics simulation and design, 2016.

[50] P. Spalart, S. Allmaras, A one-equation turbulence model for aerodynamic flows, La Recherce Aerospatiale 1 (1992) 5–21.

[51] D. Wilcox, Turbulence Modeling for CFD, no. v. 1 in Turbulence Modeling for CFD, DCW Industries, 2006.
URL `https://books.google.co.uk/books?id=tFNNPgAACAAJ`

[52] Riemann Solvers and Numerical Methods for Fluid Dynamics: A Practical Introduction, Springer-Verlang, New York, 1999.

[53] Y. Saad, A flexible inner-outer preconditioned gmres algorithm, SIAM Journal on Scientific Computing 14 (2) (1993) 461–469. `arXiv:https://doi.org/10.1137/0914028`, `doi:10.1137/0914028`.
URL `https://doi.org/10.1137/0914028`

[54] W. F.M., Viscous Fluid Flow, McGraw-Hill, New York.

[55] R. Schaback, H. Wendland, Characterization and construction of radial basis functions, in: V. U. Press (Ed.), Curve and Surface Fitting: Saint Malo 1999, 2000, pp. 1–16.

[56] D. N. Penenberg, Mathematical Statistics: Basic Ideas and Selected Topics, 2nd edn, vols I and II P. J. Bickel and K. A. Doksum, 2015 Boca Raton, Chapman and Hall–CRC xxii + 548 pp., $99.95 (vol. I); 438 pp., $99.95 (vol. II) ISBN 978-1-498-72380-0, Vol. 179, 2016. `arXiv:https://rss.onlinelibrary.wiley.com/doi/pdf/10.1111/rssa.12217`, `doi:https://doi.org/10.1111/rssa.12217`.
URL `https://rss.onlinelibrary.wiley.com/doi/abs/10.1111/rssa.12217`

[57] R. Dwight, Robust mesh deformation using the linear elasticity equations, in: H. Deconinck, E. Dick (Eds.), Computational Fluid Dynamics 2006, Springer Berlin Heidelberg, Berlin, Heidelberg, 2009, pp. 401–406.

[58] D. Liu, V. Toropov, D. C. Barton, O. M. Querin, Weight and mechanical performance optimization of blended composite wing panels using lamination parameters, Structural and Multidisciplinary Optimization 52 (2015) 549–562. doi:10.1007/S00158-015-1244-X.

[59] E. Carrera, A. Varello, L. Demasi, A refined structural model for static aeroelastic response and divergence of metallic and composite wings, CEAS Aeronautical Journal 4. doi:10.1007/s13272-013-0063-2.
URL https://doi.org/10.1007/s13272-013-0063-2

[60] Z. Siddiqi, J. Lee, A computational fluid dynamics investigation of subsonic wing designs for unmanned aerial vehicle application, Proceedings of the Institution of Mechanical Engineers, Part G: Journal of Aerospace Engineering 233 (2019) 095441001985255. doi:10.1177/0954410019852553.

[61] M. Drela, Xfoil: An analysis and design system for low reynolds number airfoils, Vol. 54, 1989. doi:10.1007/978-3-642-84010-4_1.

[62] H. M.J., R. R. R., G. G.M., Effects of grit roughness and pitch oscillations on the naca 4415 airfoil, Golden, CO: National Renewable Energy Laboratory.

[63] W. Haase, V. Selmin, B. Winzell, Progress in Computational Flow-Structure Interaction: Results of the Project UNSI, supported by the European Union 1998 – 2000, Notes on Numerical Fluid Mechanics and Multidisciplinary Design, Springer Berlin Heidelberg, 2013.
URL https://books.google.co.uk/books?id=Yg0ACQAAQBAJ

[64] H. Versteeg, W. Malalasekera, An Introduction to Computational Fluid Dynamics: The Finite Volume Method, Pearson Education Limited, 2007.
URL https://books.google.co.uk/books?id=RvBZ-UMpGzIC

[65] Q. Wen, X. He, Z. Lu, R. Streiter, T. Otto, A comprehensive review of miniatured wind energy harvesters, Nano Materials Science 3 (2) (2021) 170–185. doi:https://doi.org/10.1016/j.nanoms.2021.04.001.
URL https://www.sciencedirect.com/science/article/pii/S2589965121000180

[66] A. Pagani, E. Carrera, Large-deflection and post-buckling analyses of laminated composite beams by carrera unified formulation, Composite Structures 170 (2017) 40–52. doi:https:

//doi.org/10.1016/j.compstruct.2017.03.008.
URL https://www.sciencedirect.com/science/article/pii/S0263822317306499

[67] B. Wu, A. Pagani, M. Filippi, W. Chen, E. Carrera, Large-deflection and post-buckling analyses of isotropic rectangular plates by carrera unified formulation, International Journal of Non-Linear Mechanics 116 (2019) 18–31. doi:https://doi.org/10.1016/j.ijnonlinmec.2019.05.004.
URL https://www.sciencedirect.com/science/article/pii/S0020746219302653

[68] C. Howcroft, D. Calderon, L. Lambert, M. Castellani, J. E. Cooper, M. H. Lowenberg, S. Neild, Aeroelastic Modelling of Highly Flexible Wings, 2016. arXiv:https://arc.aiaa.org/doi/pdf/10.2514/6.2016-1798, doi:10.2514/6.2016-1798.
URL https://arc.aiaa.org/doi/abs/10.2514/6.2016-1798

[69] E. Carrera, M. Filippi, E. Zappino, Free vibration analysis of rotating composite blades via carrera unified formulation, Composite Structures 106 (2013) 317–325. doi:https://doi.org/10.1016/j.compstruct.2013.05.055.
URL https://www.sciencedirect.com/science/article/pii/S0263822313002791

[70] M. L. Ribeiro, G. orio F.O. Ferreira, R. de Medeiros, A. onio J.M. Ferreira, V. Tita, Experimental and numerical dynamic analysis of laminate plates via carrera unified formulation, Composite Structures 202 (2018) 1176–1185, special issue dedicated to Ian Marshall. doi:https://doi.org/10.1016/j.compstruct.2018.05.085.
URL https://www.sciencedirect.com/science/article/pii/S0263822318301703

[71] D. Massegur, D. Clifford, A. Da Ronch, S. Symon, Comparing reduced order model forms for nonlinear dynamical systems, 33rd Congress of the International Council of the Aeronautical Sciences.

[72] Y. Amini, H. Emdad, M. Farid, An accurate model for numerical prediction of piezoelectric energy harvesting from fluid structure interaction problems, Smart Materials and Structures 23 (9) (2014) 095034. doi:10.1088/0964-1726/23/9/095034.
URL https://doi.org/10.1088/0964-1726/23/9/095034

[73] H. Mutsuda, Y. Tanaka, R. Patel, Y. Doi, Y. Moriyama, Y. Umino, A painting type of flexible piezoelectric device for ocean energy harvesting, Applied Ocean Research 68 (2017) 182–193.

doi:https://doi.org/10.1016/j.apor.2017.08.008.
URL https://www.sciencedirect.com/science/article/pii/S0141118717302419